Swift and *XMM–Newton* observations of an RS CVn-type eclipsing binary SZ Psc: superflare and coronal properties

Subhajeet Karmakar [1,2,3]★ Sachindra Naik [2] Jeewan C. Pandey [3] and Igor S. Savanov[4]

[1]*Monterey Institute for Research in Astronomy (MIRA), 200 Eighth Street, Marina, CA 93933, USA*
[2]*Astronomy & Astrophysics Division, Physical Research Laboratory, Navrangapura, Ahmedabad 380009, India*
[3]*Aryabhatta Research Institute of Observational Sciences (ARIES), Manora Peak, Nainital 263002, India*
[4]*Institute of Astronomy, Russian Academy of Sciences, ul. Pyatniskaya 48, Moscow 119017, Russia*

ABSTRACT

We present an in-depth study of a large and long duration (>1.3 d) X-ray flare observed on an RS CVn-type eclipsing binary system SZ Psc using observations from *Swift* observatory. In the 0.35–10 keV energy band, the peak luminosity is estimated to be 4.2×10^{33} erg s^{-1}. The quiescent corona of SZ Psc was observed $\sim$5.67 d after the flare using *Swift* observatory, and also $\sim$1.4 yr after the flare using the *XMM–Newton* satellite. The quiescent corona is found to consist of three temperature plasma: 4, 13, and 48 MK. High-resolution X-ray spectral analysis of the quiescent corona of SZ Psc suggests that the high first ionization potential (FIP) elements are more abundant than the low-FIP elements. The time-resolved X-ray spectroscopy of the flare shows a significant variation in the flare temperature, emission measure, and abundance. The peak values of temperature, emission measure, and abundances during the flare are estimated to be 199 ± 11 MK, $2.13 \pm 0.05 \times 10^{56}$ cm^{-3}, 0.66 ± 0.09 Z$_\odot$, respectively. Using the hydrodynamic loop modelling, we derive the loop length of the flare as $6.3 \pm 0.5 \times 10^{11}$ cm, whereas the loop pressure and density at the flare peak are derived to be $3.5 \pm 0.7 \times 10^3$ dyn cm^{-2} and $8 \pm 2 \times 10^{10}$ cm^{-3}, respectively. The total magnetic field to produce the flare is estimated to be 490 ± 60 G. The large magnetic field at the coronal height is supposed to be due to the presence of an extended convection zone of the subgiant and the high orbital velocity.

Key words: stars: activity – stars: coronae – stars: flare – stars: individual (SZ Psc) – stars: magnetic field – X-rays: stars.

1 INTRODUCTION

Our current understanding of the mechanisms of stellar flares is developed based on the Sun. Stellar flares generally occur close to the active regions. Coronal plasma near the active regions confines in closed magnetic structure called 'loop'. The loops have a localized magnetic field of the order of a few kilo-Gauss and extend from the lower atmosphere of these active regions to coronal heights. The chromospheric footpoints of these loops are jostled by convective motions, whereas the loops get twisted and distorted depending on the local conditions until they undergo a magnetic reconnection process near the loop tops (Parker 1988). The reconnection process results in a rapid and transient release of magnetic energy in the stellar corona, and the event is termed a flare. The flaring event is also associated with the acceleration of charged particles, which gyrate downward along the magnetic field lines producing synchrotron radio emissions. When these ionized beams collide with denser material at the chromospheric footpoints, hard X-ray photons are emitted. This also heats the chromospheric footpoints up to tens of MK, causing evaporation of material from the lower atmosphere. As a result, the density in the newly formed coronal loop is increased and emitted in soft X-ray and extreme UV wavelengths.

Flares produced by the RS Canum Venaticorum (RS CVn) type binaries show many analogies with the solar flares (Hall 1976). These binaries are close but detached systems, typically consisting of a G–K giant/subgiant and a late-type main-sequence/subgiant companion. Based on the rotation period (P), the RS CVn binaries are subdivided into three following categories: short-period ($P \leq 1$ d), classical (1 d $\leq P < 14$ d), and long-period ($P \geq 14$ d) binaries. The tidal forces between the components of the RS CVn binaries can cause the rotational period to be synchronized with the orbital period. Moreover, a thicker convection zone of the evolved giant/subgiant component leads to a much higher level of magnetic activities in RS CVn binaries than in the Sun and other late-type stars. Analysis of flares in cool giants and subgiants is therefore very important as it gives us an opportunity to probe the structure and dynamic behaviour of the corona of RS CVn binaries, which in principle can be significantly different from the corona of dwarf stars. Due to the lower surface gravity in the cool giants and subgiants than in the cool main-sequence stars, a larger scale height is yielded, which possibly allows a very extended corona to develop (Ayres et al. 2003).

In this paper, we investigate a long-duration flaring event observed on an active, bright RS CVn-type partial eclipsing double-line spectroscopic binary system SZ Psc. The system consists of a spotted chromospherically active K1 IV subgiant with a radius 5.1 R$_\odot$ and mass 1.62 M$_\odot$ and a less active F8 V companion with a radius 1.50 R$_\odot$ and mass 1.28 M$_\odot$ (Jakate et al. 1976). Due to the higher brightness level, the K1 IV subgiant is considered as the primary,

★ E-mail: subhajeet09@gmail.com, sk@mira.org

whereas the less luminous but comparatively hotter F8 V companion is considered as the secondary. The primary subgiant is filling 80–90 per cent of its Roche lobe. The system is located at a distance of $89.9^{+0.7}_{-0.6}$ pc (Bailer-Jones et al. 2018). The orbital period of the system is 3.9657 d (Eaton & Henry 2007), which is supposed to be almost synchronous with the rotational period of the components of the tidally locked system. In recent years, a tertiary component of SZ Psc system has been detected spectroscopically with the estimated mass and orbital period of 0.9 $M_\odot$ and 1283 ± 10 d, respectively (Xiang et al. 2016). The luminosity contribution of the tertiary star to the system is estimated to be 5 per cent by Xiang et al. (2016), which is in good agreement with the derived values of 3–4 per cent by Eaton & Henry (2007).

Since the first light variation was detected by Jensch (1934), SZ Psc remained an exciting source for photometric and spectroscopic observations throughout the last century (Jakate et al. 1976; Catalano et al. 1978; Tumer & Kurutac 1979; Eaton et al. 1982; Tunca 1984; Antonopoulou, Deliyannis & Mitrou 1995; Lanza et al. 2001). Starspot modelling performed on SZ Psc suggested the presence of several active regions on the surface of the cooler subgiant component (Eaton & Hall 1979; Lanza et al. 2001; Kang et al. 2003). The first Doppler images of SZ Psc were generated by Xiang et al. (2016) using high-resolution optical spectra. These images revealed that the K1 IV star exhibits pronounced high-latitude spots as well as numerous intermediate- and low-latitude spot groups during the entire observing season. High level of chromospheric activity associated with the K1 IV primary component was also demonstrated by strong chromospheric emission in Mg II h & k, Ca II H & K, Hα, and Ca II infrared-triplet lines (e.g. Jakate et al. 1976; Bopp et al. 1981; Zhang & Gu 2008; Cao & Gu 2012). Hα outbursts and flare-like events were detected by Bopp et al. (1981), Ramsey & Nations (1981), and Huenemoerder & Ramsey (1984). The flaring events on SZ Psc in the ultraviolet waveband were observed by Doyle et al. (1994). The authors also found variation in Mg II strength, possibly phase-dependent, and an apparent eclipse of a plage in Mg II. However, excess absorption features in the subtracted Hα profiles caused by prominence-like material have been discussed by Zhang & Gu (2008) and Cao & Gu (2012). Several optical chromospheric activity indicators were analysed by Cao et al. (2019) using the spectral subtraction technique, and during their observation, a series of possibly associated magnetic activity phenomena, including flare-related prominence activation, optical flare, and post-flare loops, were detected. The corona of SZ Psc was studied for the first time by Walter & Bowyer (1981) in soft X-ray band using the imaging proportional counter (IPC) of the *Einstein Observatory*. The authors also demonstrated that the RS CVn systems, as a class, are the producers of copious soft X-ray emissions. In recent years, X-ray flaring activity has been observed on SZ Psc using the Gas Slit Camera (GSC) of the Monitor of All-sky X-ray Image (MAXI). From the observations on 2009 September 28, Tsuboi et al. (2016) analysed a flare observed on SZ Psc in 2–20 keV energy range with the flare energy of 5×10^{32} erg s^{-1}. On 2011 November 5, another flare was detected with a larger X-ray luminosity of 3×10^{33} erg s^{-1} (Negoro et al. 2011). These detections of large flaring events show that the corona of SZ Psc is active. Therefore, further investigation of the extreme events in SZ Psc would help us understand the dynamic behaviour of the corona of an evolved RS CVn-type binary system.

In this paper, we present a detailed time-resolved analysis of an X-ray superflare observed on SZ Psc using the *Neil Gehrels Swift Observatory* (hereafter *Swift*). We have also used the observations from the *XMM–Newton* observatory obtained almost 1.4 yr after the flaring event. This flare is identified as one of the largest and longest-

duration flares ever observed on SZ Psc. We have organized the paper as follows: The observations and data reduction procedure are discussed in Section 2. The light curves and the phase-folded light curves have been discussed in Section 3 and Section 4, respectively. We discussed the spectral analysis of the quiescent corona and the time-resolved analysis of the flaring corona in Section 5. The loop modelling has been presented in Section 6, whereas the coronal loop-properties are described in Section 7. Finally, in Section 8, we have discussed our results and presented the conclusions.

2 OBSERVATIONS AND DATA REDUCTION

We have used X-ray, UV, and optical observations of SZ Psc using *Swift* and *XMM–Newton* observatories. The observations and the data reduction procedures adopted for each X-ray observatory are described below.

2.1 *Swift*

A flaring event on SZ Psc triggered *Swift*'s Burst Alert Telescope (BAT; Barthelmy et al. 2005) as an Automatic Target. All the timing analysis in this paper is referenced to the BAT trigger time 2015 January 15 UT 09:08:42 (reported by D'Elia et al. 2015; Drake et al. 2015), we refer to this as T0. In this work, we have utilized 10 observation IDs from the *Swift* observatory, which include five observation IDs for BAT, eight observation IDs for X-Ray Telescope (XRT; Burrows et al. 2005), and eight observation IDs for ultraviolet/optical telescope (UVOT; Roming et al. 2005). A detailed log of these observations is given in Table 1.

2.1.1 BAT data

The BAT is a large field of view, coded aperture imaging instrument which is highly sensitive in the 14–150 keV range. Although SZ Psc was within the field of view of BAT between T0–16.861 and T0+110.024 ks, the source was bright enough to be detectable in hard X-ray between T0–11.101 and T0+57.659 ks. In order to perform spectral analysis, the source needs to be bright enough for which spectrum can be extracted with significant counts per bin. Therefore, for spectral analysis of SZ Psc, we could only use the BAT observations from T0–0.127 to T0 + 0.957 ks. We used the standard BAT pipeline software within FTOOLS[1] version 6.29 with the latest CALDB version 'BAT (20171016)'[2] to correct the energy from the efficient but slightly non-linear energy assignment made on board. We used the `batbinevt` task to extract the light curves in the 14–150 keV range. We mask-weighted the spectra in the 14–50 keV band, generated using the `batmaskwtevt` and `batbinevt` tasks, with an energy bin of 80 channels. The BAT ray-tracing columns in spectral files were updated using the `batupdatephakw` task. We applied the systematic error vector to the spectra from the calibration data base using the `batphasyserr` task. The BAT detector response matrix was computed using the `batdrmgen` task. We created sky images in two broad energy bins using the tasks `batbinevt` and `batfftimage`. The `batcelldetect` task was used to find the flux at the source position after removing a fit to the

---

Table 1. The log of observations of SZ Psc from *Swift* and *XMM–Newton* observatories.

Observatory	Obs. ID	Obs. Start time (UTC)	Phase^a (ϕ)	Exposure time (ks)				Offset (arcmin)
Swift				BAT	XRT	UVOT		
	00030738051	2015-01-15 04:27:58	0.954	6.98	–	–		3.41
	00625898000	2015-01-15 08:52:56	0.143	12.52	5.31	4.91		3.41
	00625898001	2015-01-15 17:04:57	0.226	0.18	2.00	1.99		2.05
	00625898002	2015-01-16 01:06:59	0.310	0.15	2.00	1.99		2.23
	00084556002	2015-01-16 03:00:58	0.335	0.12	–	–		2.23
	00625898003	2015-01-16 04:10:29	0.343	–	1.99	1.98		1.74
	00625898004	2015-01-16 07:37:31	0.378	–	1.99	1.97		0.62
	00625898005	2015-01-16 14:10:20	0.447	–	2.00	1.99		0.23
	00033606001	2015-01-21 00:54:59	0.569	–	0.22	0.22		3.94
	00033606002	2015-01-21 00:59:59	0.570	–	2.00	1.98		5.88
XMM–Newton				PN	MOS	RGS	OM	
	0785140201	2016-05-26 20:49:07	0.594	13.47	13.65	13.78	3.89	0.05

Note. ^{a}The phase is computed corresponding to the start time of each observation ID. The ephemeris has been adopted from Eaton & Henry (2007).

diffuse background and the contribution of bright sources in the field of view. The spectral analysis of all the BAT spectra was carried out in 14–50 keV range using the XSPEC package (version[3] 12.12.0; Arnaud 1996).

2.1.2 XRT data

After the trigger, a slew placed the source in the apertures of the narrow-field instrument XRT, which started observing SZ Psc from T0+0.381 ks. From the beginning of the XRT observation of SZ Psc till ∼T0+110 ks, there are several data gaps mostly within the range of 15 min to 1.5 h, except for three occasions where the data-gaps are for 3.5, 4.5, and 7.4 h. After T0 + 110 ks, *Swift* returned again to the field of SZ Psc after 5.67 d (i.e T0+488.981 ks) and observed until T0 + 495.881 ks. During the ∼500 ks of total *Swift*/XRT observation, excluding the data gaps, SZ Psc has a net effective exposure time of ∼17.5 ks.

The XRT observation of SZ Psc was in the energy range of 0.3–10 keV, using CCD detectors with an energy resolution of ≈140 eV at the Fe K (6 keV) region. However, in this study, we have ignored data in the 0.3–0.35 keV range due to the known charge trapping effects of the XRT (Pagani et al. 2011). We used the *Swift* xrtpipeline task (version 0.13.6) to produce the cleaned and calibrated event files. All the data were reduced using the latest calibration files from the CALDB version 'XRT (20210915)' release.[4] The cleaned event lists generated with this pipeline are free from the effects of hot pixels and the bright Earth.

As SZ Psc was very bright in X-rays during the flare, the data were recorded in Windowed Timing (WT) mode throughout the XRT observations. From the cleaned event list, images, light curves, and spectra for each observation were obtained using XSELECT (version V2.4m) package.[5] We used grade 0–2 events in WT mode to optimize the effective area and hence the number of collected counts. As the peak count rate of the WT mode data of SZ Psc is less than 100 counts per second, it was not necessary for further analysis to correct the data for pile-up (Romano et al. 2006). The WT

mode data give a one-dimensional image strip. In order to extract the source products, we considered a rectangular 40 × 20 pixel region, i.e. 40 pixels long along the image strip and 20 pixels wide (where 1 pixel corresponds to 2.36 arcsec). In order to extract the background products, we selected a 40 × 20 pixel rectangular region in the fainter end of the image strip. Taking into account the mirror effective area, filter transmission, vignetting correction, and point spread function correction (PSF; Moretti et al. 2005) as well as the exposure map correction, the *ancillary response files* for the WT mode were generated using the task xrtmkarf. In order to perform the spectral analysis, we used the latest *response matrix files* (Godet et al. 2009), i.e. swxwt0to2s6_20131212v015.rmf for WT mode. All the XRT spectra were binned to contain more than 20 counts per bin using the grppha task. The spectral analysis of all the XRT spectra was carried out in an energy range of 0.35–10 keV using XSPEC.

2.1.3 UVOT data

The *Swift*/UVOT began observing SZ Psc from T0 + 0.363 ks in all six filters, which include three optical filters (i.e. *U*, *B*, and *V*) and three UV filters (i.e. *UVW1*, *UVW2*, *UVM2*). Among the UV filters, the image observed with the *UVW1* filter is completely saturated, whereas the images observed with the *UVM2* and *UVW2* filters are partially saturated. The useful non-saturated observations with the *UVM2* filter were found between T0+28.795 and T0 + 494.879 ks. Similarly, for the *UVW2* filter, the observations between T0 + 490.065 and T0 + 495.824 ks were found to be unsaturated. The images observed with the *U*, *B*, and *V* optical filters were not saturated during the flare peak. However, SZ Psc was not observed in any of the optical filters after T0 + 12.141 ks. The data reduction was performed using the latest calibration files from the CALDB version 'UVOT (20201215)' release.[6] In order to perform photometry for the non-saturated images, we used a circular region of 30 arcsec radius co-axially centred on the intensity peaks. We also considered another circular region of the same radius from a blank area of the sky near the source position. The light curves were extracted using the uvotmaghist task.

---

[3]https://heasarc.gsfc.nasa.gov/xanadu/xspec/
[4]For latest CALDB versions, please see https://heasarc.gsfc.nasa.gov/docs/heasarc/caldb/swift/
[5]See https://swift.gsfc.nasa.gov/analysis/

[6]For latest CALDB versions, please see https://heasarc.gsfc.nasa.gov/docs/heasarc/caldb/swift/

2.2 *XMM–Newton*

Approximately 1.4 yr after T0, *XMM–Newton* observation of SZ Psc was carried out on 2016 May 26 UT 20:49:07 (PI. Schmitt, J; ID: 0785140201). *XMM–Newton* satellite has onboard three co-aligned X-ray telescopes (Jansen et al. 2001) and one co-aligned 30-cm optical/UV telescope, also known as optical monitor (OM; Mason et al. 2001). The X-ray telescopes consist of three European Photon Imaging Cameras (EPIC; Strüder et al. 2001; Turner et al. 2001), and two Reflection Grating Spectrometers (RGS; Den Herder et al. 2001). For the first ∼10 ks, SZ Psc was simultaneously observed with EPIC and RGS instruments, whereas the source was observed with all the instruments (EPIC, RGS, and OM) only for the last ∼4 ks. A log of the *XMM–Newton* observation is given in Table 1.

2.2.1 *EPIC data*

The EPIC instrument onboard *XMM–Newton* satellite contains two nearly-identical MOS 1 and MOS 2 (Turner et al. 2001) detectors and one PN (Strüder et al. 2001) detector. It provides imaging and spectroscopy in the energy range of 0.15–15 keV with an angular resolution of 4.5–6.6 arcsec and a spectral resolution ($E/\Delta E$) of 20–50. SZ Psc was observed for ∼14 ks using EPIC PN, MOS 1, and MOS 2 detectors. The EPIC data were reduced using standard *XMM–Newton* SCIENCE ANALYSIS SYSTEM (SAS) software[7] version 20.0.0, utilizing the latest version of calibration files. The pipeline processing of raw EPIC *observation data files* (ODFs) was done using the epchain and emchain tasks, which allow calibrations both in energy and astrometry of the events registered in each CCD chip. We restricted our analysis to the 0.35–10 keV range as the background contribution is particularly relevant at high energies, where stellar sources have very little flux and are often undetectable. Event list files were extracted using the SAS task evselect. We used the epatplot task to check for pile-up effects and found that the data are not affected due to photon pile-up and high background proton flare. The background was chosen from several source-free regions on the detectors around the source. We used epiclccorr task to correct for the good time intervals, dead time, exposure, PSF, quantum efficiency, and background subtraction. We used the SAS task especget to generate the spectra, which also computes the photon redistribution as well as the ancillary matrix. Finally, the spectra were rebinned to have a minimum of 20 counts per spectral bin using FTOOLS task grppha. The spectral analysis of EPIC data has been carried out using XSPEC in an energy range of 0.35–10 keV.

2.2.2 *RGS data*

The RGS consists of two identical grating spectrometers: RGS 1 and RGS 2. These spectrometers share about half of the photons in the converging beams that feed the X-ray telescopes with MOS 1 and MOS 2 detectors. In each spectrometer, the dispersed photons are recorded by a strip of eight CCD MOS chips. One of these chips has failed in each of the spectrometers, leading to gaps in the spectra. However, these gaps affect different spectral regions. SZ Psc was observed simultaneously with EPIC and RGS instruments for ∼14 ks. The RGS instrument provides spectral resolution of ≈70–500 from 5–35 Å (0.35–2.5 keV). In order to reduce the RGS data, we used SAS task rgsproc. Standard processing was performed for

spectral extraction and response matrix generation. In order to extract light curves, we used the SAS task rgslccor. Using the FTOOLS task grppha, all RGS spectra were binned to contain more than 10 counts per bin. The spectral analysis of RGS data has been carried out using XSPEC in an energy range of 0.35–2.5 keV.

2.2.3 *OM data*

The OM observation of SZ Psc was started on 2016 May 26 UT 23:52:30, which is ∼10 ks after the beginning of the EPIC and RGS observations. The OM telescope module consists of a modified 30 cm Ritchey–Chretien telescope with a focal ratio of f/12.7. The wavelength coverage is between 170 and 650 nm in a 17 arcmin square field of view. The OM has six broadband filters (*U*, *B*, *V*, *UVW1*, *UVM2*, and *UVW2*), one white, one magnifier, and two grisms (UV and optical). SZ Psc was observed only in the *UVW2* filter for ∼4 ks until 2016 May 27 UT 00:57:31. The OM data for SZ Psc only contained image mode and fast mode data. The OM data have been processed by the SAS tasks omichain[8] and omfchain[9] for reducing the image mode and fast mode data, respectively. The light curve is extracted from the fast-mode data. The mean background-subtracted source count rate is estimated to be 40.7 count s^{-1}, whereas the background count rate is estimated to be 0.3 count s^{-1}.

3 LIGHT CURVES

3.1 Hard X-ray light curve

The hard X-ray light curve in the 14–150 keV energy range obtained from *Swift* BAT is shown in the top panel of Fig. 1. The inset in the panel shows a close-up view of the BAT light curve for the time interval marked by the rectangular region. The vertical blue dashed line shows the trigger time. The blue shaded region shows the time interval for which only BAT observation is available. The green and orange shaded regions show the time intervals for which both BAT + XRT observations are available. SZ Psc was significantly bright in hard X-ray from ∼T0–0.127 ks. While the flare triggered BAT at T0, the BAT count rate reached up to 0.005 ± 0.001 count s^{-1}. After the trigger, the BAT count rate gradually increased for ∼1 ks and reached a maximum count rate of 0.006 ± 0.001 count s^{-1}. However, after a gap of ∼1 ks, the count rate was found to have dropped and reached only ≲0.001 count s^{-1}. During the rest of the observation, the BAT light curve either shows detections with large uncertainties (∼0.002–0.003 count s^{-1}) with a poor signal-to-noise ratio (S/N ratio ∼1–1.3) or shows non-detection with the upper limit ranging from ∼0.001–0.003 count s^{-1}. Therefore, the data quality does not allow us to identify any variability or non-variability of the BAT light curve from T0 + 0.957 ks to the end of the observation.

3.2 Soft X-ray light curve

The 0.35–10 keV soft X-ray light curve obtained from *Swift* XRT observations of SZ Psc is shown in Fig. 1(b). The inset in Fig. 1(b) shows the close-up view of the XRT light curve for the same time interval as shown in the close-up view of the BAT light curve in Fig. 1(a). The *Swift* XRT observed the flare on SZ Psc from T0 + 0.381 ks in the WT mode, with an initial XRT count rate of ∼79 count s^{-1}. The XRT count rate increased up to ∼92 count s^{-1} until the

---

[7]See SAS threads at https://www.cosmos.esa.int/web/xmm-newton/sas-threads

[8]https://www.cosmos.esa.int/web/xmm-newton/sas-thread-omi
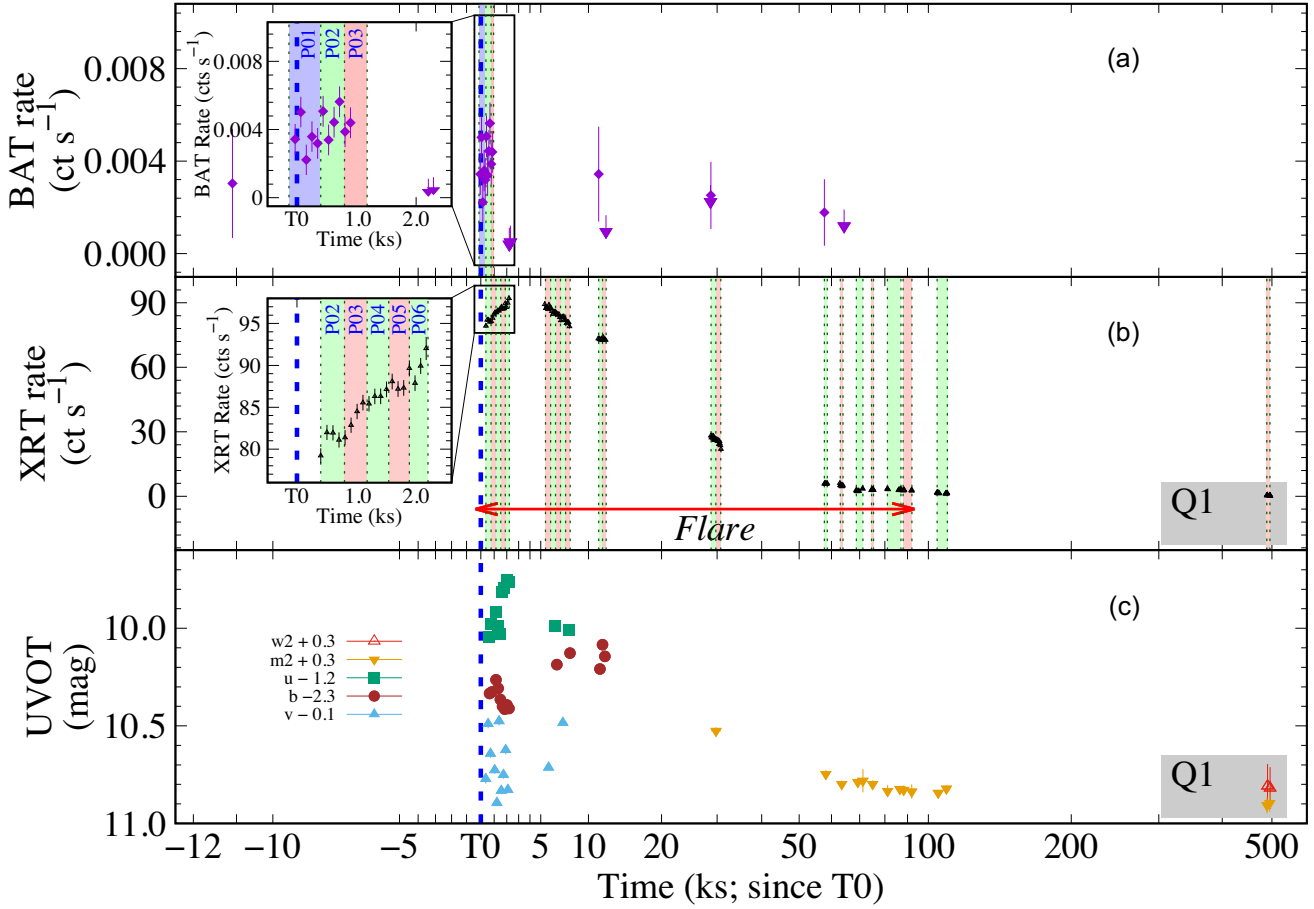[9]https://www.cosmos.esa.int/web/xmm-newton/sas-thread-omf

Figure 1. *Swift* light curve of SZ Psc is shown. From top to bottom panels: (a) BAT, (b) XRT, and (c) UVOT light curves are shown. Temporal binning for BAT light curves is 50 s, whereas the binning for XRT light curves is 200 s. The BAT light curve was extracted in the 14–150 keV energy band, whereas the XRT light curve was extracted in the 0.35–10 keV band. The non-saturated UVOT light curves for two UV filters (*UVW2*, *UVM2*) and three optical filters (*U*, *B*, *V*) are shown in the bottom panel. The blue dashed vertical line in each panel indicates the trigger time, whereas the black dotted vertical lines show the time intervals for which time-resolved spectroscopy was performed. The blue shaded region shows the segment for which only BAT spectral analysis is performed. The alternate orange and green shaded regions show the segments for which XRT (and XRT + BAT, wherever available) spectral analysis has been performed. The insets in panels (a) and (b) are the close-up views of the segments. The details of the close-up view are given in the text. The red horizontal arrow in panel (b) indicates the tentative duration of the flare in the soft X-ray energy band. The grey shaded regions in panels (b) and (c) show the quiescent state segment Q1, which has been analysed in Section 5.

observation was interrupted at around T0 + 2.21 ks due to the orbit of the *Swift* satellite. Although the XRT count rate showed an upward trend, the simultaneous BAT observations indicated that SZ Psc was already faint in hard X-ray. After 3.24 ks of data-gap, while *Swift* XRT started observing SZ Psc, the source was showing a decay from an initial count rate of ~90 count s^{-1}. Until T0 + 7.971 ks, the XRT count rate decreased to ~79 count s^{-1}. The *Swift* XRT count rate was found to decline rapidly and dropped to 28 count s^{-1} by T0 + 30 ks, whereas the count rate was ~6 count s^{-1} by T0+57 ks. After a gap of ~16 ks, the XRT observations for the time interval T0+58 to T0 + 92 ks showed a much slower decay of the flare during which the count rate decreased from ~7 to 3 count s^{-1}. After ~109 ks from T0, the soft X-ray count rate decreased to 1.3 count s^{-1}. The *Swift* returned to the field of SZ Psc after 5.67 d from the trigger, where the XRT count rate had dropped to ~0.5 count s^{-1}. This epoch is shown with a grey shaded rectangle and marked as 'Q1' in Fig. 1, and appears to represent the quiescent corona of SZ Psc.

Due to the presence of data gaps in the light curves, it is difficult to confirm whether this is a single flaring event that occurred on SZ Psc.

For our analysis, however, we assume that the data from the *Swift* observations correspond to a single flare. The flare also shows an exponential rise and exponential decay. The e-folding rise time (τ_r) and decay time (τ_d) of the flare in the XRT band are derived to be 14.4 ± 0.5 and 21.4 ± 0.3 ks, respectively. This shows a sharp rise and slow decay of the flare. Both of these values are comparable to or more than those of the observed flares in other G-K dwarfs, RS CVn binaries, and dMe stars (e.g. Schmitt 1994; Osten & Brown 1999; Pandey & Singh 2012). The flare duration is estimated to be >1.3 d, which is among the longest duration X-ray flares ever observed on SZ Psc.

The background-subtracted 0.35–10 keV EPIC PN light curve of SZ Psc is shown in the top panel of Fig. 2. In the second panel from the top, we plotted the MOS 1 + MOS 2 (= MOS, hereafter) light curve in the same energy band. In the third panel of Fig. 2, 0.35–2.5 keV X-ray light curve obtained from combined RGS instruments (= RGS 1 + RGS 2) is shown. All of these light curves indicate that SZ Psc remained at a constant flux level during the ~14 ks of observation in the soft X-ray energy band. In order to compare the
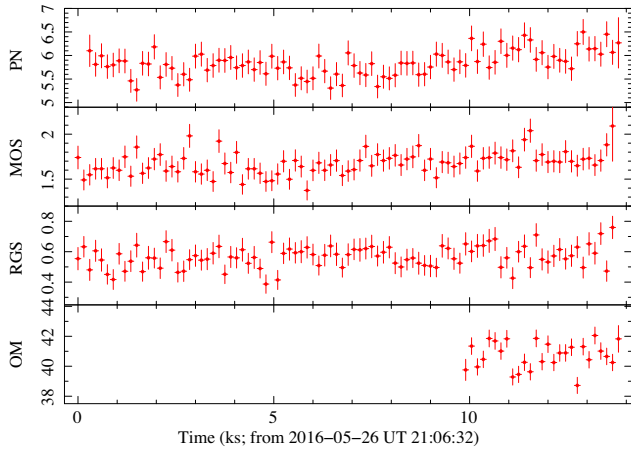
Figure 2. The *XMM–Newton* light curves of the Q2 segment have been shown. The light curves obtained from EPIC PN, EPIC MOS, RGS, and OM instruments are shown from top to bottom panels, respectively. All the light curves are binned at 150 s. In the bottom panel, the UV light curve obtained from the OM observation is in the *UVW2* filter.

XMM–Newton observation with the *Swift* observations, we converted the *XMM–Newton* PN count rate to an equivalent *Swift* WT count rate using the Mission Count Rate Simulator `webpimms`[10] (version PIMMS v4.11b). The corona of SZ Psc is assumed to consist of astrophysical plasma. For the conversion, we used the coronal temperature components of SZ Psc as estimated in this study and described in Section 5.1. We found that the converted count rate of *XMM–Newton* PN is comparable within the 1σ uncertainty level of the XRT count rate during the Q1 segment. Although the *XMM–Newton* observation was carried out $\sim$1.4 yr after T0, due to the comparable count rate with the Q1 epoch, we consider this segment as the quiescent corona of SZ Psc and term it as the 'Q2' segment.

3.3 UV and optical light curve

The bottom panel of Fig. 1 shows the UV and optical light curves obtained from the *Swift* UVOT instruments. For most of the UV and optical filters, the error bars are smaller than the size of the symbols. Since all the images obtained using the *UVW1* filter were heavily saturated, we could not extract light curves of SZ Psc for this filter. The images obtained with *UVM2* filter were not saturated from T0 + 28.790 ks till the end of the UVOT observation. Observations with *UVM2* filter show magnitude variation from 10.2 to 10.5 mag, indicating the late decay phase of the flare. Although the *UVM2* light curve seems to show an exponential decay in the later phase of the flare, we could not estimate the decay time since we do not have the information of the flare peak in this filter. The *UVW2* observations were not saturated only in the quiescent segment 'Q1'. During the observation, the *UVW2* magnitude was found to be constant at 10.5 ± 0.1 mag.

Among all the optical observations with *Swift* observatory, *U*- and *V*-band light curves covered until T0+7.7 and T0 + 7.3 ks, whereas *B*-band light curve had a longer coverage until T0 + 11.9 ks. The magnitudes of *U*-, *B*-, and *V*-band light curves varied in the range of 11.2–10.9, 12.7–12.4, and 11.0–10.6 mag. The *U*-band light curve showed a clear rise and decay phase, and the light curve seemed to

---

[10] see https://heasarc.gsfc.nasa.gov/cgi-bin/Tools/w3pimms/w3pimms_pro.pl for latest version of `WEBPIMMS`

---

follow the soft X-ray light curve, whereas the *B*- and *V*-band light curves showed a lot of scatter, and it is difficult to understand the time behaviour in *B* and *V* optical bands. Due to the data gap and absence of observations in the later part of the flare, a reliable estimation of e-folding decay time was not possible in any of the optical bands. During the Q2 segment, SZ Psc was also observed in UV with the OM instrument of the *XMM–Newton* satellite. The observation was carried out only in *UVW2* waveband and is shown in the bottom panel of Fig. 2. This shows that the *UVW2*-band light curve remains constant during the Q2 segment.

4 PHASE-FOLDED LIGHT CURVE

As SZ Psc is an eclipsing binary, there is a certain chance that the *Swift* observations of the flare could have been affected due to the eclipse. In order to identify whether the flare is eclipsed or not, we phase folded the light curve using the ephemeris HJD = 2,449,284.4483 + 3.96566356 × phase, adopted from Eaton & Henry (2007). Fig. 3 shows phase-folded light curves obtained from the XRT observations of SZ Psc in WT mode (solid red triangles). For comparison, we also plotted the phase-folded ΔV magnitude from earlier observations and shown on the right-hand *y*-axis. The solid grey circles and solid green line represent the observations and modelled light curve of SZ Psc from Eaton & Henry (2007), whereas the black open circles and solid light-blue line represent the same for the observations from Eaton et al. (1982). The solid purple line is the modelled light curve for a completely unspotted K star as adopted from fig. 2 of Eaton & Henry (2007). We also plotted the *Swift* XRT equivalent of the *XMM–Newton* PN detector data (count rate) from the segment Q2 using the open blue diamond in Fig. 3. The bottom-right inset shows the close-up view of the phase range 0.56–0.64. We find that the flare peak and the decay of the flare are completely outside the eclipse. The peak of the flare was observed in the 0.14–0.2 phase range. We also identified that the XRT observations got over at phase 0.45, which possibly coincided with the end of the flare (i.e. T0 + 110 ks). Therefore, the entire flaring episode occurred outside the primary and secondary eclipses. We also identify that the Q1 (observed with *Swift*) and Q2 (observed with *XMM–Newton*) segments are at phase ranges of 0.56–0.59 and 0.59–0.64, respectively. Therefore, both of these segments are also out of the secondary eclipse phase.

5 X-RAY SPECTRAL ANALYSIS

In the following section, we provide a detailed description of the X-ray spectral analysis carried out in this work. The spectra for two quiescent segments, Q1 and Q2, have been analysed independently, whereas time-resolved spectroscopy is performed during the flare. All the uncertainties in the spectral fitting are estimated with a 68 per cent confidence interval ($\Delta\chi^2 = 1$), equivalent to $\pm 1\sigma$. In our analysis, the solar photospheric abundances ($Z_\odot$) were adopted from Anders & Grevesse (1989), whereas to model N_H, we used the photoionization cross-sections obtained by Wilms, Allen & McCray (2000).

5.1 Quiescent spectra

5.1.1 *Swift* XRT spectrum of Q1

The *Swift* XRT spectrum corresponding to the Q1 segment is shown in Fig. 6 with grey asterisks. The 0.35–10 keV spectrum is fitted with the *Astrophysical Plasma Emission Code* (`apec`; Smith et al. 2001)
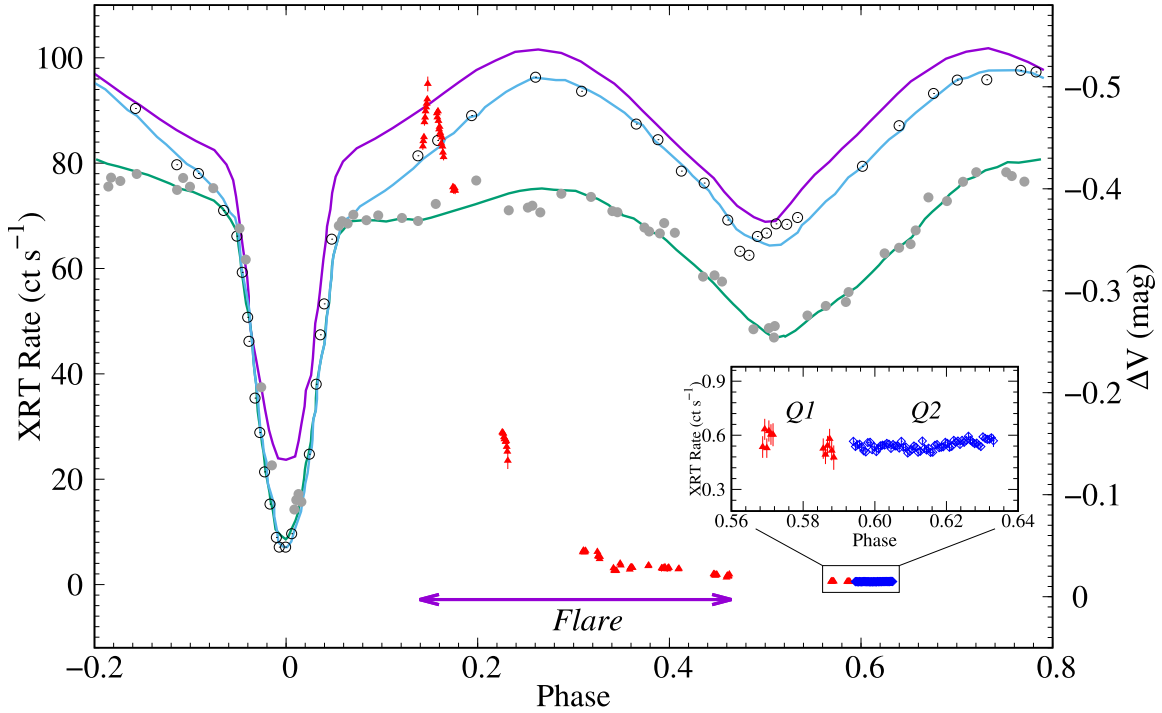
Figure 3. Change in soft X-ray count rate and *V*-band magnitude of SZ Psc with orbital phase is shown. The left- and right-hand sides along *y*-axis in the figure indicate the *Swift* XRT count rate and differential *V*-band magnitude, whereas the *x*-axis shows the phase of SZ Psc. Data from *Swift* XRT observations in WT mode are shown in solid red triangles. Earlier optical observations of SZ Psc are plotted for the same phase in the right-hand *y*-axis. The solid grey circles and solid green line represent the observations and modelled light curve of SZ Psc from Eaton & Henry (2007), whereas the black open circles and solid light-blue line represent the same for the observations from Eaton et al. (1982). The solid purple line is the modelled light curve for a completely unspotted K star as adopted from fig. 2 of Eaton & Henry (2007). The purple horizontal line represents the phase range during which the flare on SZ Psc was observed with the *Swift* observatory. This shows that the flare is out of eclipse. The quiescent observations (Q1 and Q2) from the *Swift* and *XMM–Newton* observations are found to be in the close phase range. The inset in the figure shows the zoomed version of the quiescent phase-folded light curve.
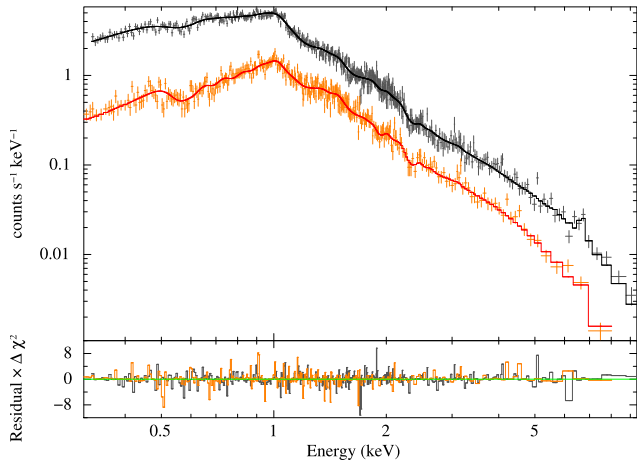

Figure 4. The *XMM–Newton* EPIC PN + MOS simultaneous spectra of SZ Psc for the segment Q2 is shown along with the best-fitting 3-T apec model. The grey and orange points in the figure correspond to the data from the PN and MOS instruments, respectively. The black and red solid lines in the upper panel show the corresponding best-fitting 3-T apec models. The bottom panel shows the residuals in units of $\Delta \chi^2$. The best-fitting parameters are given in Table 2.

available in XSPEC. In order to estimate the hydrogen column density, we used the *Tuebingen–Boulder ISM absorption model* (tbabs; Wilms et al. 2000). Initially, the spectrum of the Q1 segment was fitted with a single (1-T), double (2-T), and triple (3-T) temperature plasma model with solar abundances. None of the plasma models (1-T, 2-T, or 3-T) were found to be acceptable with solar photospheric abundances due to large values of χ^2. In the next stage, the global abundance (Z) was left as a free parameter. We found that both the 2-T and 3-T plasma models with the subsolar abundances fitted well, yielding χ^2 within the acceptable range. However, spectral fitting with the 3-T model was relatively better than the 2-T model with an F-test value of 1.14 and an F-test probability of 66.7 per cent. Therefore, from the spectral analysis of the *Swift* XRT data, the quiescent corona of SZ Psc seems to be represented by the three temperatures plasma. The estimated temperature components are >0.18, 1.1 ± 0.1, and >3.27 keV, whereas the corresponding Emission Measures (EMs) are estimated to be <1.17 × 10^{54}, $0.9^{+0.4}_{-0.3}$ × 10^{54}, and $0.3^{+0.2}_{-0.1}$ × 10^{54} cm^{-3}. The best-fitting value of global abundances was estimated to be $0.07^{+0.09}_{-0.03}$ Z$_\odot$. In our analysis, N$_H$ was a free parameter, and its value was estimated to be 6^{+7}_{-5} × 10^{20} atoms cm^{-2}. Within a 0.1 deg cone in the direction of SZ Psc, the survey of HI4PI Collaboration (2016) suggests that the expected average Galactic H I column density to be 4.8 ± 0.1 × 10^{20} atoms cm^{-2}, which is consistent with our estimated value. The best-fitting 3-T plasma model, along with the residuals, is shown with a solid black line in Fig. 6. The best-fitting values of the derived parameters for all three models are given in the second, third, and fourth columns of Table 2. In order to estimate the unabsorbed luminosities of individual

Table 2. The best-fitting parameters obtained from the spectral fitting of quiescent corona (Q1 and Q2 segments) of SZ Psc. The best-fitting parameters obtained from fitting apec 1-T, apec 2-T, and apec 3-T models to the Q1 (*Swift* XRT spectra) and Q2 (*XMM–Newton* EPIC PN+MOS spectra) segments are given below.

Parameters	Q1 (XRT)[a]			Q2 (PN+MOS)[b]		
	APEC-1T	APEC-2T	APEC-3T	APEC-1T	APEC-2T	APEC-3T
N_H (10^{20} atoms cm^{-2})	$2.38^{+0.02}_{-0.01}$	4.3 ± 4.2	6^{+7}_{-5}	2.41	$2.4^{+0.4}_{-0.3}$	3.3 ± 0.5
kT_1 (keV)	$1.5^{+0.2}_{-0.3}$	$0.98^{+0.08}_{-0.12}$	>0.18	1.47	1.024 ± 0.008	0.36 ± 0.03
EM_1 (10^{54} cm^{-3})	1.3 ± 0.3	$1.0^{+0.5}_{-0.6}$	<1.17	1.62	1.1 ± 0.2	0.29 ± 0.08
$\log_{10}(L_{X1}$ in erg s$^{-1})$	30.99 ± 0.02	30.80 ± 0.03	$30.1^{+0.1}_{-0.2}$	31.08	30.873 ± 0.007	30.07 ± 0.01
kT_2 (keV)	–	>3.21	1.1 ± 0.1	–	$4.2^{+0.5}_{-0.3}$	1.13 ± 0.02
EM_2 (10^{54} cm^{-3})	–	$0.3^{+0.3}_{-0.1}$	$0.9^{+0.4}_{-0.3}$	–	0.44 ± 0.09	0.9 ± 0.2
$\log_{10}(L_{X2}$ in erg s$^{-1})$	–	30.72 ± 0.05	30.74 ± 0.03	–	30.761 ± 0.008	30.818 ± 0.007
kT_3 (keV)	–	–	>3.27	–	–	$4.1^{+0.5}_{-0.3}$
EM_3 (10^{54} cm^{-3})	–	–	$0.3^{+0.2}_{-0.1}$	–	–	0.44 ± 0.09
$\log_{10}(L_{X3}$ in erg s$^{-1})$	–	–	$30.73^{+0.04}_{-0.05}$	–	–	30.767 ± 0.008
Z ($Z_\odot$)	$0.04^{+0.04}_{-0.03}$	$0.06^{+0.08}_{-0.03}$	$0.07^{+0.09}_{-0.03}$	0.08	0.076 ± 0.007	0.11 ± 0.01
$\log_{10}(L_X$ in erg s$^{-1})$	30.99 ± 0.02	31.06 ± 0.02	31.08 ± 0.02	31.08	31.122 ± 0.007	31.133 ± 0.007
χ^2(DOF)	1.702 (35)	1.215 (33)	1.208 (31)	2.606 (992)	1.103 (987)	0.993 (985)

Notes. The distance of SZ Psc is considered as $89.9^{+0.7}_{-0.6}$ pc, estimated by Bailer-Jones et al. (2018) using *Gaia* DR2 observations. All the errors shown in this table are in a 68 per cent confidence level.
The luminosities L_{X1}, L_{X2}, L_{X3}, and L_X are derived in the 0.35–10 keV energy range.
[a]*XMM–Newton* observation was carried out at 2016-05-26 T21:06:32 during the phase range 0.59–0.64.
[b]*Swift* observations were carried out at 2015-01-15 T09:08:42 during the phase range 0.56–0.59. The best fit was derived in the energy range 0.35–10 keV.
N_H, kT, and EM are the Galactic H I column density, plasma temperature, and emission measures, respectively. Z is the global metallic abundances relative to the solar photospheric abundances (Anders & Grevesse 1989).

temperature components, as well as the total unabsorbed luminosity of the quiescent corona of SZ Psc, we used the cflux model.[11] The unabsorbed luminosity for the Q1 segment is estimated to be $10^{31.08 \pm 0.02}$ erg s^{-1}. The luminosities corresponding to the first, second, and third temperature components are estimated to be 0.1, 0.5, and 0.4 times the total luminosity.

5.1.2 XMM–Newton *EPIC spectra of Q2*

SZ Psc was observed simultaneously with three EPIC detectors (i.e. PN, MOS 1, and MOS 2). As MOS 1 and MOS 2 are identical detectors and do not show any difference in the spectra of SZ Psc, we extracted the combined spectra of MOS 1 + MOS 2 (= MOS) and used them for further spectral analysis. Since both of the EPIC instruments have a similar spectral resolution, the simultaneous spectral fitting has been performed for the EPIC PN and MOS spectra. Fig. 4 shows PN and MOS spectra of the Q2 segment using grey and orange plus symbols. Initially, the spectra were fitted with 1-T, 2-T, and 3-T plasma models with solar abundances, which did not give an acceptable fit. When we let the global abundances vary freely, it converges to a subsolar value and gives a better fit. However, the 1-T plasma model with subsolar abundances does not give an acceptable fit. Although 2-T and 3-T plasma models both give a fit within the acceptable range, we found the 3-T model is relatively better than the 2-T model, with an F-test value of 54.5 and F-test probability >99.9 per cent. The fifth, sixth, and seventh columns of Table 2 summarize the best-fitting values of the derived parameters for all three models. The best-fitting temperatures have been estimated as 0.36 ± 0.03, 1.13 ± 0.02, and $4.1^{+0.5}_{-0.3}$ keV. The corresponding

emission-measures were estimated to be $0.29 \pm 0.08 \times 10^{54}$, $0.9 \pm 0.2 \times 10^{54}$, and $0.44 \pm 0.09 \times 10^{54}$ cm^{-3}. The spectral fitting also gives an estimation of the global metallic abundance to be 0.11 ± 0.01 Z$_\odot$. Since these values are similar to those estimated from the spectral fitting of the Q1 segment, it is more likely that the corona of SZ Psc was in a similar activity level during Q1 and Q2 segments. This finding is important, as Q1 and Q2 segments were observed ∼1.4 yr apart. This also suggests that both Q1 and Q2 correspond to the quiescent corona of SZ Psc. It is noteworthy that the PN + MOS joint spectral fitting was performed with the *XMM–Newton* data, which had better statistics than the *Swift* XRT data. The derived parameters for Q2 segments were also more precise than those estimated for the Q1 segment of *Swift* XRT. Therefore, for further analysis, we have considered the parameters estimated from the Q2 segment as the quiescent parameters. The best-fitting 3-T models for the PN and MOS detectors are shown with the black and red solid lines in the upper panel of Fig. 4, respectively. The bottom panel of Fig. 4 shows the residuals from the best-fitting models.

5.1.3 XMM–Newton *RGS spectra of Q2*

Simultaneously observed high-resolution RGS spectra of the Q2 segment in the 0.35–2.5 keV energy band are useful for estimating the elemental abundances and plasma density. In the left-hand panel of Fig. 5, the first-order spectra of RGS 1 and RGS 2 are shown with light-blue and orange plus symbols. At the same time, the right-hand panel of Fig. 5 shows the second-order spectra with the same colours and symbols. The emission lines are identified and marked with black arrows. Strong emission lines of iron, neon, oxygen, nitrogen, and magnesium are clearly detectable. We carried out simultaneous spectral analysis of both the orders of RGS 1 and RGS 2 data. In order to perform the spectral fitting, we used a 3-T *Variable*

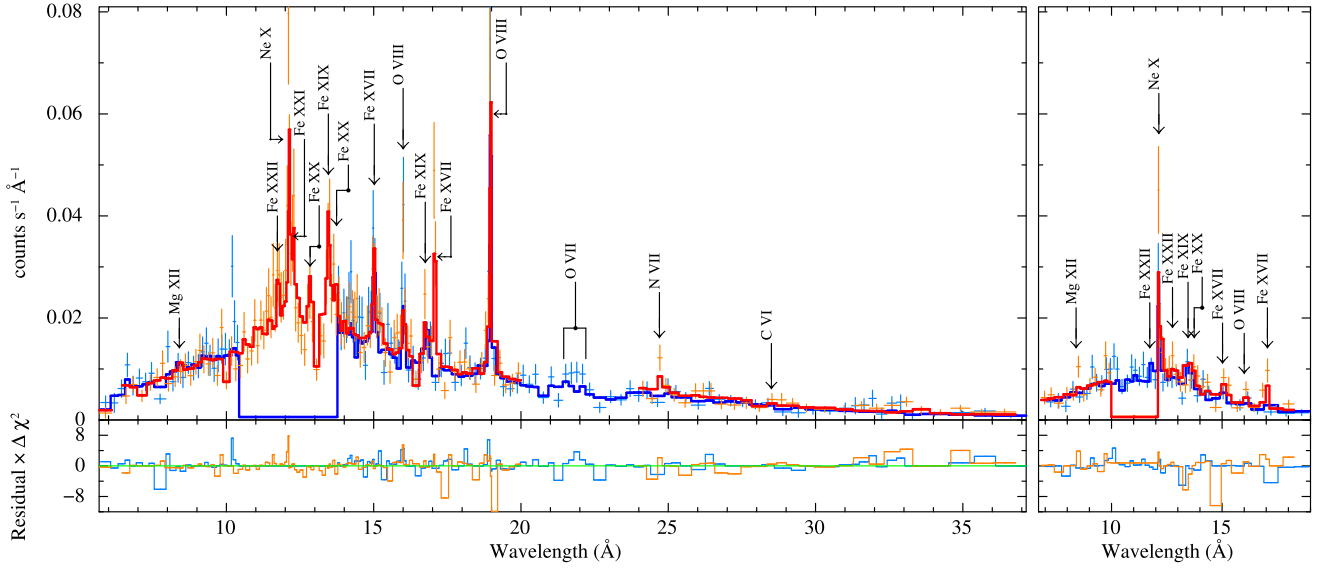[11]For cflux model please see https://heasarc.gsfc.nasa.gov/xanadu/xspec/manual

Figure 5. Time-integrated high-resolution *XMM–Newton* RGS spectra of the quiescent segment (Q2) have been shown. The top-left panel shows the first-order spectra of RGS 1 (light-blue plus symbol) and RGS 2 (orange plus symbol). The top-right panel shows the second-order spectra with the same symbols. A simultaneous spectral fitting of RGS 1 + RGS 2, first order + second order, has been performed. The best-fitting 3-T *V*apec models are shown with blue and red solid lines for RGS 1 and RGS 2, respectively. The black arrows indicate the emission lines of different elements in different ionization states. The bottom panels of each figure show the corresponding residuals in the unit of $\Delta\chi^2$.
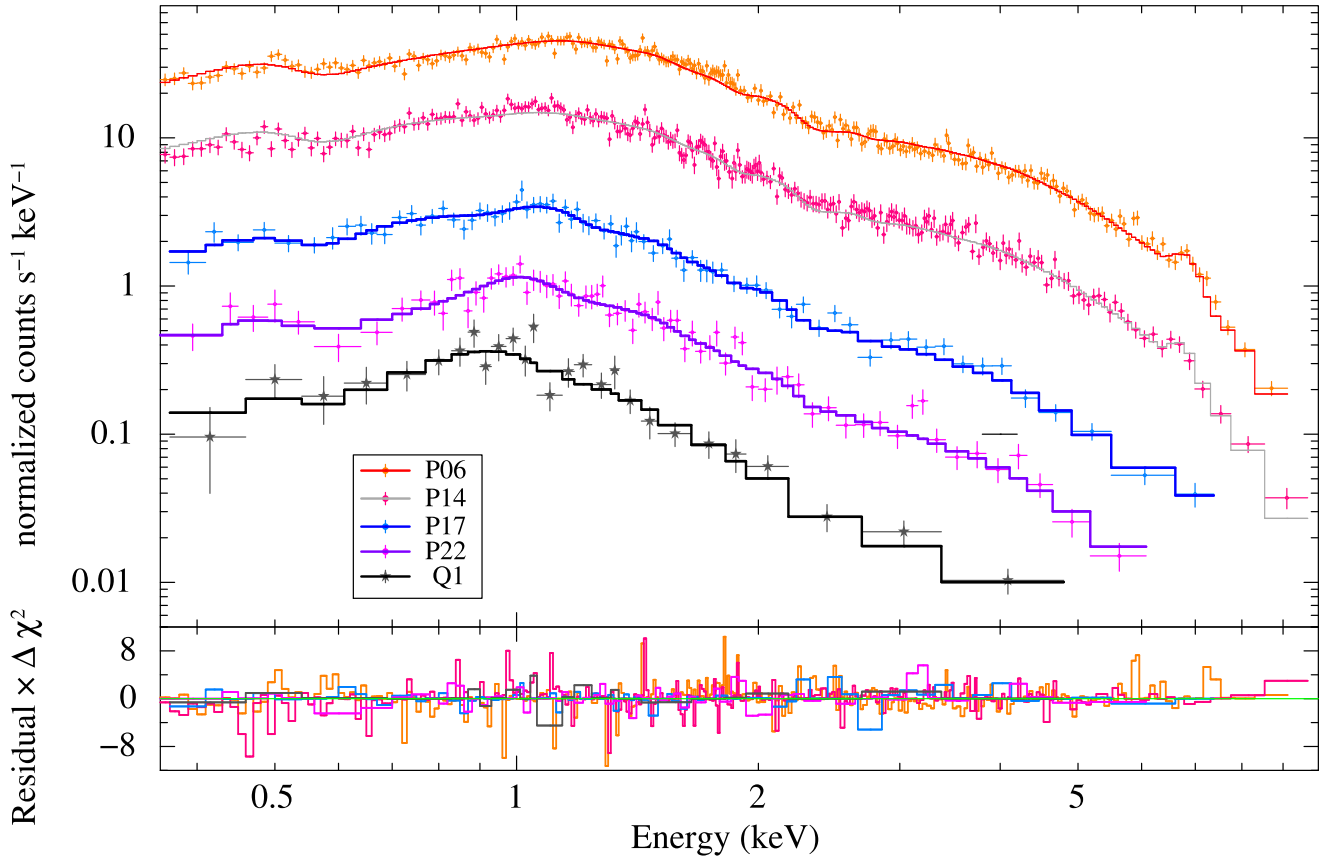
Figure 6. Time-resolved XRT spectra of SZ Psc in 0.35–10 keV range are shown. The grey asterisks in the top panel show the spectra for the quiescent phase Q1 best fitted with a 3-T apec model, where the model parameters have been shown in Table 2. All other spectra are the representative flare spectra of different time segments, as mentioned in the inset of the top panel. The spectra corresponding to the flare segments are best fitted with a 4-T apec model as described in Section 5.2 and given in Table 4. (Please also see the *online-only material* of this paper, where the *Swift* XRT time-resolved spectra of all the segments have been shown along with the best-fitting models).
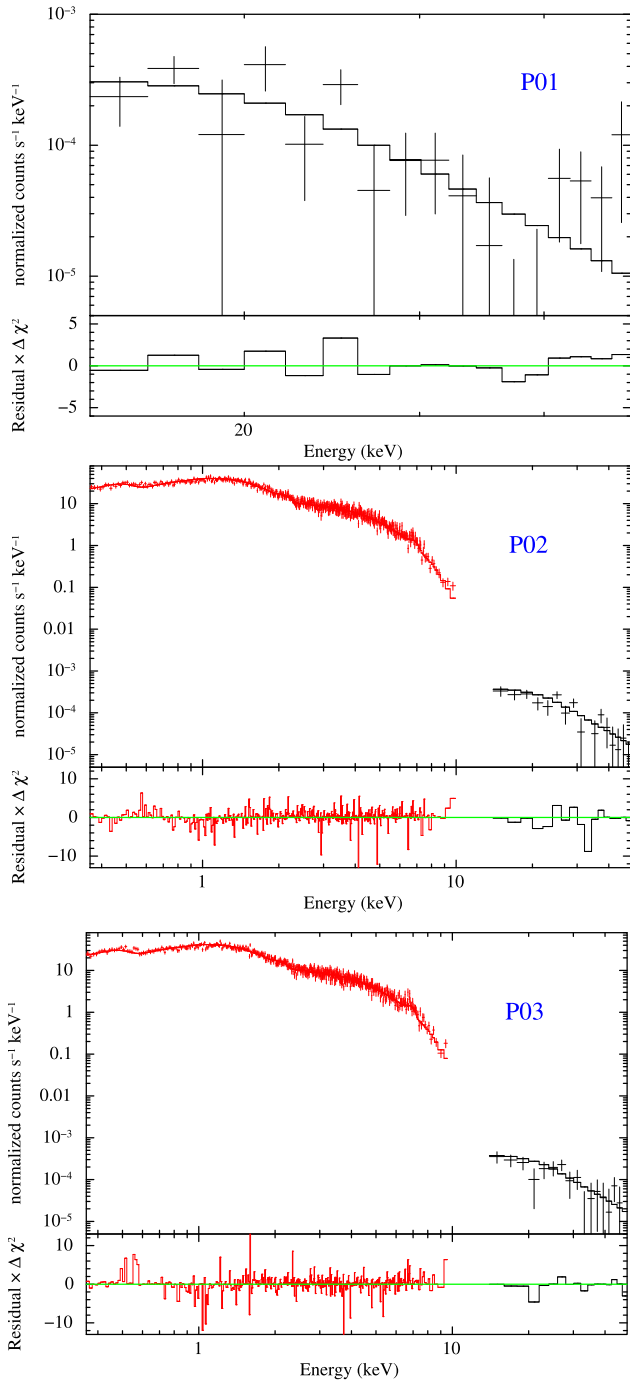
Figure 7. Spectral fitting of the *Swift* BAT and XRT + BAT data. The figure at the top shows the BAT spectra for segment P01. The middle and bottom figures show the combined XRT and BAT spectra for the segments P02 and P03, respectively. In the top panel of each figure, the spectra and the best-fitting 4-T model are shown. The bottom panel of each figure shows the corresponding residuals.

Astrophysical Plasma Emission Code (*V*apec; Smith et al. 2001). We fixed the temperatures, emission measures, and the N_H as derived from the EPIC PN + MOS simultaneous spectral fitting. The metallic abundances of helium, carbon, nitrogen, oxygen, neon, magnesium, silicon, sulfur, argon, calcium, iron, and nickel were allowed to vary freely and independently. Table 3 shows the derived parameters from

Table 3. Spectral parameters of SZ Psc for the quiescent phase Q2, derived from the *XMM–Newton* RGS spectra.

Parameters	Values	Parameters	Values
N_H (10^{20} cm^{-2})	3.34	$\log_{10}(L_X$ in erg s^{-1})	30.971 ± 0.009
kT_1 (keV)	0.36	EM_1 (10^{54} cm^{-3})	0.29
kT_2 (keV)	1.13	EM_2 (10^{54} cm^{-3})	0.90
kT_3 (keV)	4.06	EM_3 (10^{54} cm^{-3})	0.44
He	$0.46^{+0.05}_{-0.07}$	Si	<0.19
C	<0.30	S	<0.31
N	0.3 ± 0.1	Ar	<0.37
O	0.10 ± 0.01	Ca	<0.08
Ne	0.28 ± 0.04	Fe	0.076 ± 0.006
Mg	0.20 ± 0.06	Ni	0.2 ± 0.1
χ^2(DOF)	1.114 (819)		

Note. We have adopted the distance of SZ Psc as $89.9^{+0.7}_{-0.6}$ pc, estimated by Bailer-Jones et al. (2018) using *Gaia* DR2 observations. All the errors shown in this table are for a 68 per cent confidence interval. Abundances relative to solar photospheric (Anders & Grevesse 1989). The luminosities L_X are derived in the 0.35–2.5 keV energy range.

the spectral fitting. The best-fitting models are shown in the top panel of Fig. 5, using blue and red solid lines for RGS 1 and RGS 2, respectively. The bottom panel shows the residual in the unit of $\Delta\chi^2$. We have discussed it further in Section 8.4.

Using the *XMM–Newton* RGS spectra, we also investigated the electron densities of coronal plasma from the density-sensitive line ratios of forbidden to inter-combination lines of the helium-like triplets of O VII (Gabriel & Jordan 1969). If the electron collision rate is sufficiently high, the ions in the upper level of the forbidden transition do not return to the ground level radiatively. Instead, the ions are collisionally moved to the upper level of the inter-combination transitions, from where they eventually decay radiatively to the ground state. Therefore, the resulting ratio of the forbidden to the inter-combination line (*f/i*) is sensitive to density. As the He-like triplet of Ne IX and O VII were not strong enough in the RGS spectra of the quiescent corona of SZ Psc, we could not estimate the precise coronal density by this method.

5.2 Flare spectra: time-resolved spectroscopy

In order to study the temporal evolution of the stellar parameters during the flare, we performed a time-resolved spectral analysis using *Swift* data. The entire flare duration is divided into 22 time segments and are shown by vertical shaded regions in Fig. 1. These divisions are chosen in such a way that each segment contains a sufficient and similar number of total counts. The length of the time bins varies from 0.33 to 5.95 ks. Among those segments, one segment (P01) has BAT observation but no XRT observation, two segments (P02 and P03) have both XRT and BAT observations, whereas 19 segments (P04–P22) have only XRT observations. The P01 segment that corresponds to only BAT observation is shown with the blue shaded vertical region in the top panel of Fig1. All other segments are shown with alternate green and orange shaded vertical regions in the top two panels of Fig. 1. The time intervals for which the X-ray spectra were accumulated are given in the second column of Table 4. In this section, we discuss XRT, BAT, and XRT + BAT spectral analysis separately.

Table 4. Time-resolved spectral parameters during the flare event of SZ Psc.

Parts	Time interval (ks)	kT_4 (keV)	EM_4 (10^{55} cm^{-3})	Z ($Z_\odot$)	$\log_{10}(L_x)$ (in cgs)	χ^2 (DOF)
P01[a]	T0−0.127 : T0 + 0.381	14^{+6}_{-4}	18^{+11}_{-7}	0.41^b	$33.06^{+0.06}_{-0.07}$	1.136 (15)
P02[c]	T0+0.381 : T0 + 0.771	$15.5^{+0.6}_{-0.5}$	19.5 ± 0.5	$0.44^{+0.13}_{-0.12}$	33.768 ± 0.007	1.053 (532)
P03[c]	T0+0.771 : T0 + 0.957	15.0 ± 0.6	20.0 ± 0.5	0.57 ± 0.13	33.784 ± 0.007	1.125 (528)
P02	T0 + 0.381 : T0 + 0.771	$17.1^{+1.1}_{-0.9}$	$19.8^{+0.6}_{-0.5}$	0.41 ± 0.14	33.574 ± 0.007	1.028 (515)
P03	T0 + 0.771 : T0 + 1.151	15.7 ± 0.8	20.1 ± 0.5	$0.57^{+0.14}_{-0.13}$	33.592 ± 0.007	1.133 (511)
P04	T0 + 1.151 : T0 + 1.521	$14.5^{+0.7}_{-0.6}$	20.7 ± 0.5	0.52 ± 0.12	33.602 ± 0.007	1.035 (513)
P05	T0 + 1.521 : T0 + 1.881	$14.1^{+0.7}_{-0.9}$	21.3 ± 0.5	0.43 ± 0.11	33.606 ± 0.007	1.079 (505)
P06	T0 + 1.881 : T0 + 2.211	15.0 ± 0.8	21.2 ± 0.5	0.62 ± 0.14	33.619 ± 0.007	1.107 (494)
P07	T0 + 5.451 : T0 + 5.941	$12.9^{+1.3}_{-0.2}$	$19.9^{+0.7}_{-0.4}$	0.57 ± 0.09	33.595 ± 0.007	1.285 (553)
P08	T0 + 5.941 : T0 + 6.441	11.6 ± 0.4	19.4 ± 0.4	0.52 ± 0.08	33.578 ± 0.007	1.187 (550)
P09	T0 + 6.441 : T0 + 6.951	$12.0^{+0.5}_{-0.4}$	19.0 ± 0.4	0.56 ± 0.09	33.574 ± 0.007	0.964 (553)
P10	T0 + 6.951 : T0 + 7.471	11.8 ± 0.4	18.8 ± 0.4	0.49 ± 0.08	33.563 ± 0.007	1.051 (545)
P11	T0 + 7.471 : T0 + 7.971	11.3 ± 0.4	17.7 ± 0.4	0.66 ± 0.09	33.550 ± 0.007	1.077 (539)
P12	T0 + 11.231 : T0 + 11.691	12.4 ± 0.5	16.5 ± 0.4	0.53 ± 0.10	33.510 ± 0.007	1.179 (509)
P13	T0 + 11.691 : T0 + 12.141	10.5 ± 0.4	16.1 ± 0.3	0.57 ± 0.09	33.497 ± 0.007	1.110 (503)
P14	T0 + 28.790 : T0 + 29.750	7.8 ± 0.3	5.9 ± 0.1	0.42 ± 0.06	33.040 ± 0.007	1.133 (441)
P15	T0 + 29.750 : T0 + 30.770	7.5 ± 0.2	5.7 ± 0.1	0.44 ± 0.06	33.015 ± 0.007	0.987 (440)
P16	T0 + 57.686 : T0 + 58.666	5.1 ± 0.3	1.10 ± 0.04	$0.35^{+0.09}_{-0.07}$	32.294 ± 0.009	1.020 (198)
P17	T0 + 62.976 : T0 + 63.966	$5.0^{+0.4}_{-0.3}$	0.99 ± 0.04	0.42 ± 0.06	32.221 ± 0.009	0.785 (173)
P18	T0 + 68.743 : T0 + 71.233	$5.3^{+0.7}_{-0.6}$	0.41 ± 0.02	0.20 ± 0.05	31.91 ± 0.01	1.427 (106)
P19	T0 + 74.523 : T0 + 75.383	4.3 ± 0.4	0.61 ± 0.03	0.06 ± 0.05	31.98 ± 0.01	0.926 (99)
P20	T0 + 81.038 : T0 + 86.988	4.7 ± 0.4	0.51 ± 0.03	0.25 ± 0.05	31.98 ± 0.01	1.016 (139)
P21	T0 + 87.968 : T0 + 91.998	$3.8^{+0.6}_{-0.5}$	0.51 ± 0.05	0.17 ± 0.08	31.93 ± 0.01	0.875 (77)
P22	T0 + 104.574 : T0 + 110.024	$5.0^{+0.7}_{-0.5}$	0.22 ± 0.01	0.15 ± 0.03	31.68 ± 0.01	0.969 (113)

Notes. All the errors shown in this table are for a 68 per cent confidence interval. The spectral fitting is performed in the 0.35–10 keV range for XRT observations (fourth row to end of the table).
[a]In this time segment, only BAT spectra are available and fitted with an `apec` 4-T plasma model. The L_x for this segment indicates the derived luminosity corresponding to the 14–50 keV range.
[b]Abundances in this time segment are fixed at the nearest abundance value of segment P02 as derived from fitting the XRT spectra.
[c]In these time segments, XRT + BAT spectra are fitted with an `apec` 4-T plasma model. The L_x in this segment indicates the derived luminosity corresponding to the 0.35–50 keV range.

5.2.1 XRT spectral analysis

The *Swift* XRT spectra for a few representative time intervals[12] during the flare and the quiescent Q1 are shown in Fig. 6. The spectral evolution is clearly visible throughout the flare. The X-ray emission during the flaring event has a contribution from both the flare and quiescent emission. Therefore, in order to estimate the 'effective' contribution only from the flare, we performed spectral analysis by taking into account the quiescent emission as the frozen background emission. We fitted a four-temperature (4-T) astrophysical plasma model (`apec`) to each of the flare segments keeping the first three temperature components fixed to the quiescent values as estimated in Section 5.1. A 4-T plasma model gives the best fit with the reduced χ^2 in the acceptable range. Initially, in the spectral fitting, the N_H was a free parameter. The value of N_H was found to be constant during the flare and comparable with the quiescent state value (within a 1σ uncertainty level). Therefore, in the next stage of spectral fitting, N_H was fixed to the quiescent state value along with the parameters of the first three temperature components. The time evolution of derived spectral parameters is shown in Fig. 8, and the values are given in Table 4. The temperature, corresponding emission measure,

and abundances were found to vary during the flare. The peak value of global abundances (Z) was derived to be 0.66 ± 0.09 Z$_\odot$ which is ∼11 times that of the minimum value observed towards the end of the flare. The flare temperature (kT_4) peaked at a value of $17.1^{+1.1}_{-0.9}$ keV, which is ∼3.4 times that derived at the end of the flare. The corresponding emission measure (EM_4) was found to follow the flare light curve, and the highest value was derived to be $2.13 \pm 0.05 \times 10^{56}$ cm^{-3}, which is almost 10 times the minimum value observed at the end of the flare. The peak X-ray luminosity of the flare in the 0.35–10 keV energy range was derived using the `cflux` model and found to be 4.16×10^{33} erg s^{-1}, which is ∼346 times as luminous as that of the Q1 segment. From Fig. 8, it is evident that the temperature peaks before the luminosity, emission measure, and abundances peak. This phenomenon is consistent with the idea of the hydrodynamic model (see Reale 2007). This indicates that the coherent plasma evolution and the heating cause the evaporation of the chromospheric gas and increase the metal abundances in the flaring loop.

5.2.2 Spectral analysis of BAT data

The spectral analysis of 'only BAT' spectra is performed for the segment P01 using the 4-T `apec` plasma model. As in the case of XRT spectral fitting, the first three temperature components in this fitting were frozen at the quiescent values. Due to poor statistics, it was very difficult to estimate the spectral parameters. Therefore,
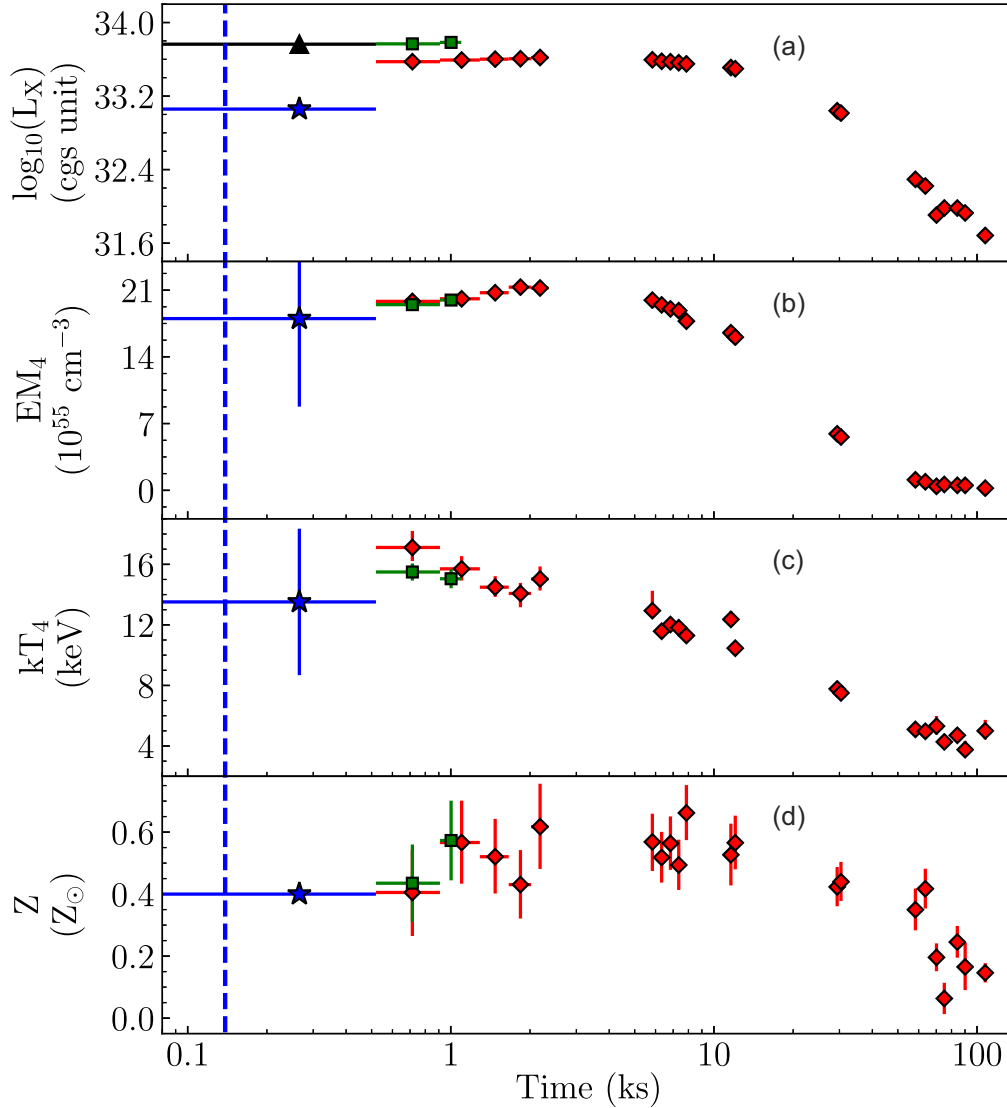
---

[12]A complete set of the best-fitting *Swift* XRT spectra corresponding to all the flare segments (P02–P22) and Q1 segment are provided in the *online-only material*.

Figure 8. The evolution of spectral parameters during the flare on SZ Psc is shown. In all the panels, the parameters derived from the BAT, XRT, and XRT + BAT spectral fitting are represented by the solid blue asterisk, solid red diamonds, and solid green squares, respectively. In the top panel (panel a), the X-ray luminosities are derived in the 0.35–10 keV (red solid diamond), 14–50 keV (blue solid star), and 0.35–50 keV (green solid squares) ranges. For the first segment, the 14–50 keV BAT luminosity is extrapolated to a 0.35–10 keV energy range (solid black triangle). Panels (b)–(d) display the variations of emission measure, plasma temperature, and abundances, respectively. The blue dashed vertical line indicates the trigger time of the flare. The horizontal bars give the time range over which spectra were extracted; the vertical bars show a 68 per cent confidence interval of the parameters.

for this analysis, we assumed that the global abundance is not very different from the nearest time segment (P02) as derived from XRT analysis. The fourth temperature and corresponding emission measure are kept as free parameters. The derived values of the temperature and emission measure are 14^{+6}_{-4} keV and $1.8^{+1.1}_{-0.7} \times 10^{56}$ cm^{-3}, respectively. We also used the cflux model to estimate the X-ray luminosity. The X-ray luminosity in the 14–50 keV range is derived to be $\sim 1.14 \times 10^{33}$ erg s^{-1}. The BAT spectra and the best-fitting model are shown in the top panel of Fig. 7. The estimated values from this analysis are given in the first row of Table 4. In Fig. 8, the BAT observations are indicated with solid blue asterisks. In order to compute the equivalent XRT luminosity in the 0.35–10 keV range, we converted the BAT luminosity using webpimms.[13] For this

conversion, the best possible multitemperature model is considered, where the three apec temperatures are taken from the three hotter components from our analysis. The equivalent X-ray luminosity in the 0.35–10 keV band is estimated to be 5.8×10^{33} erg s^{-1} and is shown with the black triangle in Fig. 8. This value is marginally higher than the luminosity during the segment P02 derived from XRT analysis.

5.2.3 XRT + BAT spectral analysis

At the beginning of the *Swift* XRT observations, SZ Psc was observed with both XRT and BAT instruments until T0+0.957 ks, which comprises two segments: P02 and P03. We carried out an XRT+BAT joint spectral fitting for these two segments. As in the case of XRT spectral analysis, the XRT + BAT observations were best fitted with a 4-T apec plasma model, keeping the first three temperature

components fixed to the quiescent values. The fourth temperature, emission measure, and global abundances are kept as free parameters. Since Galactic H I column density was not found to be variable in the 'only XRT' spectral analysis, we fixed N_H to the quiescent value. The best-fitting XRT + BAT spectra are shown in the two bottom panels of Fig. 7. In Fig. 8, the derived parameters are shown with green squares. These parameters are also given in the second and third rows of Table 4. The temperatures, emission measures, and abundances estimated from XRT + BAT analysis were found to have similar values as those derived from XRT spectral fitting within the 1σ uncertainty level. The luminosity in the 0.35–50 keV energy range was estimated to be 5.86×10^{33} and 6.08×10^{33} erg s^{-1} for the P02 and P03 segments, respectively. These values are ~1.6 times the corresponding estimated luminosities in the 0.35–10 keV energy band using only XRT observations.

6 HYDRODYNAMIC LOOP MODELLING

The magnetic loop structures of the flaring events are well studied on the Sun as they are spatially resolved. On the other hand, the stellar flares are neither spatially resolved nor direct measurements of coronal loop parameters are yet possible. Due to having several similarities of the stellar flares with the solar flares, it is possible to estimate the physical size of the loop structures involved in the stellar flares. Several approaches have been developed throughout the years to model the decay of the flares.

In this study, we used the state-of-the-art time-dependent one-dimensional hydrodynamic loop model of the stellar flares (Reale et al. 1997; Reale 2007). This model assumes that flare occurs in a single dominant loop with a constant cross-section and semicircular loop geometry. Followed by a magnetic reconnection process, a heat pulse is supposed to be released near the loop apex at the beginning of the flare. The thermodynamic cooling time-scales are proportional to the length of the flaring loop. Moreover, studies on the solar flares show that the slope (ζ) in the density–temperature plane of the flare decay path provides a diagnostic of sustained heating (Sylwester et al. 1993). The hydrodynamic model also considers the prolonged decay time-scales due to the sustained heating during the decay phase of the flare, which, in turn, provides a more realistic estimation of the flaring loop length within a single-loop scenario.

However, we know from large solar flares that the flaring events in most cases do not occur in a uniform, single, pre-defined semicircular, and steady loop as assumed in the hydrodynamic loop model of Reale et al. (1997) and Reale (2007). Instead, large flares are often associated with loop arcades of multiple loops. Therefore, for a superflare similar to that of SZ Psc, it is essential to carefully consider the applicability of the hydrodynamic loop model.

Initially, the hydrodynamic loop model was validated on 20 single-loop solar M- and C-class flares imaged by the Yohkoh SXT telescope (Reale et al. 1997). Later, this model was further applied to larger flares, including five solar X-class limb flares (Getman et al. 2011). In EUV TRACE images, those flares were found to be associated with arcades of multiple loops. In contrast to the general expectations that the single-loop model would overestimate flaring loop heights, Getman et al. (2011) found that the loop heights were comparable to or less than the individual loops measured from the TRACE images.

Further, the single-loop Hydrodynamic modelling was argued to be applicable for the multiloop arcades assuming the presence of a dominant loop (see Reale et al. 2004). However, the single-loop method was also found to be applicable in cases of multiloop structures where individual loop events have similar temporal temperature and emission measure profiles and firing nearly simultaneously (Getman
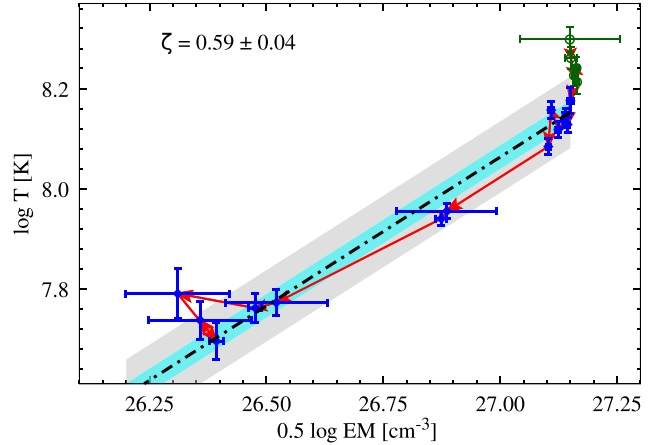
Figure 9. Evolution of the flare in [log $\sqrt{EM}$ – log T] plane. The green open circles and solid blue diamonds indicate the variation during the rising and decay phase of the flare. The red arrows indicate the chronological order in which the flare evolved in the [log $\sqrt{EM}$ – log T] plane. The black dot–dashed line shows the slope (ζ), the best fit in the decay phase of the flare. The cyan and grey shaded regions show 1σ and 3σ uncertainty levels.

et al. 2011). If the multiple individual loops are not firing near-simultaneously, it is expected to produce multimodal light curves with shorter subflare components (Aschwanden & Alexander 2001).

In this work, we understand that the frequent data gap (as shown in Fig. 1) has limited the information about the time variation during the superflare on SZ Psc. However, the light curve seems to show a long-duration and unimodal structure. Therefore, in the case of the superflare on SZ Psc, we consider that the application of the hydrodynamic loop modelling is valid, although with substantial inaccuracies.

Therefore, utilizing the empirical formula as estimated using hydrodynamic simulations (Reale 2007) the length of the flaring loop (L_{HD}) can be derived as

$$L_{HD} \text{ [cm]} = \frac{\tau_d \sqrt{T_{max}}}{1.85 \times 10^{-4} F(\zeta)} \qquad F(\zeta) \geq 1, \qquad (1)$$

where T_{max} is the maximum temperature (K) of loop apex, τ_d is the e-folding decay time (s), and $F(\zeta)$ is a non-dimensional factor that depends on the band-pass and spectral response of the instruments. For the *Swift* XRT observations, the maximum loop apex temperature T_{max} was calibrated by Osten et al. (2010) as $T_{max} = 0.0261 \times T_{obs}^{1.244}$, where both temperatures are in the unit of Kelvin. Using the peak flare temperature as estimated in Section 5.2, the maximum loop-apex temperature during the flare of SZ Psc was estimated to be 549 ± 39 MK. The factor $F(\zeta)$ was also calibrated by Osten et al. (2010) as $F(\zeta) = 1.81/(\zeta - 0.1) + 0.67$, which is valid for $0.4 \lesssim \zeta \lesssim 1.9$. These limits of applicability correspond to the heating time-scale being very long on one end and no heating on the other end.

For the *Swift* XRT observations of the flare of SZ Psc, since no density determination was available, we used the quantity $\sqrt{EM}$ as a proxy for the density, where the geometry of the flaring loop is assumed to remain constant during the decay. Fig. 9 shows the path in the [log $\sqrt{EM}$ – log T] diagram for the flare on SZ Psc. The green open circles in the diagram show the rising phase of the flare, whereas the decay phase is shown with the blue diamonds. A linear fit to the decay phase of the flare is shown with the black dot–dashed line. The uncertainties are estimated considering the uncertainties in both axes, and the 1σ and 3σ uncertainties are shown by cyan and grey-shaded regions, respectively. The slope ζ is estimated to be

0.59 ± 0.04, indicating the presence of sustained heating during the decay phase of the flare. Using above quantities and the values of τ_d mentioned in Section 3, the loop length of the flare was derived to be $6.3 \pm 0.5 \times 10^{11}$ cm using equation (1).

7 CORONAL LOOP PROPERTIES

As described in Section 6, the hydrodynamic model assumes single loop with a constant cross-section. The ratio of the loop's cross-sectional radius and the loop length ($\beta = r/L_{HD}$) is a measure of the thickness of the loop. For many solar and stellar flares the β is often fixed at $\beta = 0.1$ (see Reale et al. 1997 for solar flares; Favata et al. 2005 and Getman et al. 2008 for Orion superflares; Crespo-Chacón et al. 2007 for small stellar flare and Karmakar et al. 2017 for stellar X-ray superflares). However, recent studies have shown that β can be estimated from the data within the hydrodynamic model framework (see Getman et al. 2011; Getman, Feigelson & Garmire 2021).

The dominant cooling mechanisms of a coronal plasma are thermal conduction and radiation. The following equations show the corresponding time-scales expressed in terms of the β, loop length L_{HD}, and temporal profiles of temperature $T(t)$, X-ray luminosity $L_X(t)$, and emission measure $EM(t)$ (as adopted from Getman et al. 2011).

$$\tau_{con}(t) = \frac{3k_B}{\kappa_0 T(t)^{5/2}\beta}\sqrt{\frac{EM(t)L_{HD}}{2\pi}}, \qquad (2)$$

$$\tau_{rad}(t) = \frac{3k_B T(t)\beta}{L_{X,0.01-50}(t)}\sqrt{EM(t)2\pi L_{HD}^{3}}, \qquad (3)$$

where $\kappa_0 = 9.2\times 10^{-7}$ erg s^{-1} cm^{-1} K$^{-7/2}$ is the coefficient of thermal conductivity (Spitzer 1965) and k_B is the Boltzmann constant. A combined cooling time (τ_{th}) can be defined as an exponential folding time that combines both conduction and radiation processes, as given in the following equation:

$$\frac{1}{\tau_{th}} = \frac{1}{\tau_{con}} + \frac{1}{\tau_{rad}} \qquad (4)$$

From the equations (2), (3), and (4), the value of β can be estimated such that the combined cooling time τ_{th} would be the closest to the observed flare decay time-scale (corrected for possible sustained heating, i.e. $\tau_d/F(\zeta)$). In above equations, we have used flare emission measure and temperatures as estimated in Section 5.2 and given in Table 4. In order to estimate the X-ray luminosity in a wide energy band (i.e. 0.01–50 keV, $L_{X, 0.01-50}$), we have used the flare luminosity as given in Table 4. In order to convert the X-ray luminosity from 0.35–10 to 0.01–50 keV, we have used the multicomponent Mission Count Rate Simulator tool `webpimms`.[14] For this conversion, we have used the parameters of the three highest temperature components for each segment. Throughout the decay phase of the flare, the value of the loop thickness is found to be consistent within the limit $\beta = 0.23 \pm 0.03$, although, at flare peak, the value of the loop thickness is estimated to be $\beta_{peak} = 0.21$. Therefore, the loop volume at the flare peak is estimated to be $V = \pi \beta_{peak}^2 L_{HD}^3 = 4 \pm 1 \times 10^{34}$ cm^3.

Using the flare peak emission measure from Section 5.2, and the volume of the loop at flare peak, the density of the flaring plasma can be estimated as

$$n_e \text{ [cm}^{-3}] = \sqrt{\frac{EM_4}{V}} \qquad (5)$$

We found the density of the loop at flare peak was $8 \pm 2 \times 10^{10}$ cm^{-3}. Assuming totally ionized hydrogen plasma, from the relation $p = 2n_e kT_{max}$, the pressure in the loop is estimated to be $3.5 \pm 0.7 \times 10^3$ dyn cm^{-2} at the flare peak.

For a static non-flaring coronal loop, Rosner, Tucker & Vaiana (1978) derived a scaling law (hereafter RTV law), assuming equilibrium between a spatially uniform heating rate and the conductive and radiative loss rates. While the validity of the RTV scaling law applies to a coronal loop in hydrostatic equilibrium, Aschwanden, Stern & Güdel (2008) suggested that it might also be applicable to a flaring loop near the peak time because both the energy and momentum equations are nearly balanced near the flare peak. Therefore, using RTV scaling law, the heating rate per unit volume (HR$_V$) at the flare peak can be estimated by the following relationship:

$$\text{HR}_V \text{ [erg s}^{-1}\text{cm}^{-3}] = \frac{dH}{dVdt} \simeq 10^5 \, p^{7/6} \, L_{HD}^{-5/6} \qquad (6)$$

Utilizing the derived loop length and pressure at the flare peak, we estimated an approximate value of HR$_V$ for the flare on SZ Psc to be 0.20 ± 0.06 erg s^{-1} cm^{-3}. Using equations (5) and (6), the total heating rate (HR $= \frac{dH}{dVdt} \times V$) is estimated to be $7 \pm 1 \times 10^{33}$ erg s^{-1}, which is ~ 1.7 times than the flare maximum X-ray luminosity. The heating rate during the flare was found to be only ~ 0.4 per cent of the bolometric luminosity of the primary, whereas it was ~ 1.0 per cent of the bolometric luminosity of the secondary component of the SZ Psc system. Assuming the constant heating rate throughout the rise and decay phase of the flare, the total energy associated with the heating mechanism is estimated as $E_{tot} = (\tau_r + \tau_d) \times HR$. The total energy during the flare is derived to be $2.1 \pm 0.3 \times 10^{38}$ erg, which is also derived to be ~ 78 s of the bolometric energy output of the primary component of SZ Psc.

If the heating mechanism is responsible, the present flare is essentially due to some form of dissipation of magnetic energy. The estimated magnetic field in the newly generated loop is estimated using the equation B $= \sqrt{8\pi \, p}$, which is estimated to be 298 ± 29 G. However, if we assume that the energy released during the flare is indeed of magnetic origin, the total non-potential magnetic field B_{tot} involved in the flare energy release within an active region of the star can be estimated using the following equation:

$$E_{tot} \text{ [erg]} = \frac{(B_{tot}^2 - B^2)}{8\pi} V \qquad (7)$$

If we assume that the loop geometry does not change during the flare, using the values of E$_{tot}$, B, and V, the total magnetic field required to produce the flare is estimated to be 490 ± 60 G. The derived parameters of the flaring loop are summarized in Table 5.

8 DISCUSSION AND CONCLUSIONS

8.1 Flaring loop size and location

In this study, we carried out a detailed time-resolved spectral analysis and estimated the loop length and other flare parameters. In order to compare with other loop models, we also estimated the loop lengths using another extensively used loop model *viz.* the quasi-static loop model (Van den Oord & Mewe 1989). According to this model, the energy loss is entirely due to radiative cooling, while the conduction redistributes the energy along the loop. In the quasi-static approximation, the cooling process occurs through a sequence of stationary states of constant pressure. With the assumption of the shape of the flaring loop to be semicircular with a constant cross-section throughout the flare, the quasi-static decay time-scale

Table 5. Derived loop parameters for the flare on SZ Psc.

Ref.	Parameters	Units	Flare
1	τ_r	(ks)	14.4 ± 0.5
2	τ_d	(ks)	21.4 ± 0.3
3	$\log_{10}(L_{X, max})$	(cgs unit)	33.619 ± 0.007
4	$kT_{4, max}$	(keV)	17 ± 1
5	$EM_{4, max}$	(10^{56} cm^{-3})	2.13 ± 0.05
6	T_{obs}	(MK)	199 ± 11
7	T_{max}	(MK)	549 ± 39
8	ζ	–	0.59 ± 0.04
9	$F(\zeta)$	–	4.3 ± 0.3
10	L_{HD}	(10^{11} cm)	6.3 ± 0.5
11	L_{QS}	(10^{11} cm)	7.6 ± 0.5
12	β_{peak}	–	0.21 ± 0.03
13	V	(10^{34} cm^3)	4 ± 1
14	n_e	(10^{10} cm^{-3})	8 ± 2
15	p	(10^3 dyn cm^{-2})	3.5 ± 0.7
16	B	(G)	298 ± 29
17	HR_V	(erg s^{-1} cm^{-3})	0.20 ± 0.06
18	HR	(10^{33} erg s^{-1})	7 ± 1
19	E_{tot}	(10^{38} erg)	2.1 ± 0.3
20	B_{tot}	(G)	490 ± 60

Notes. (1, 2) – The e-folding rise and decay times, respectively, derived from the light curve.

(3) – Luminosity at the flare peak (0.35–10 keV band).

(4, 5) – Peak flare temperature and emission measure, respectively, as estimated from spectral fitting.

(6, 7) – Observed maximum temperature and loop apex temperature, respectively, in MK.

(8) – Slope of the decay path in the density–temperature diagram.

(9) – The function $F(\zeta)$ indicates the presence of sustained heating.

(10) – Length of the flaring loops estimated using hydrodynamic loop model (Reale et al. 1997).

(11) – Length of the flaring loops estimated using quasi-static loop model (Van den Oord & Mewe 1989).

(12) – Loop aspect ratio at flare peak.

(13, 14, 15) – Loop volume, density, and pressure at flare peak.

(16) – Estimated magnetic field.

(17) – Heating rate per unit volume at the flare peak.

(18) – Heating rate at the flare peak.

(19) – Total radiated energy (0.35–10 keV band).

(20) – Total magnetic field required to produce the flare.

can be estimated using equation (26) of Van den Oord & Mewe (1989). In our analysis, the quasi-static decay time-scales estimated from the EM_4 and kT_4 data were found to be similar (within 1σ uncertainty level). The quasi-static decay time was estimated to be $\sim$11.3 ks, which results in a loop length of $7.6 \pm 0.5 \times 10^{11}$ cm. This value is within the 1.3σ uncertainty level from that estimated from the hydrodynamic loop modelling as described in Section 6. However, a slightly lower value of loop length as estimated from the hydrodynamic loop modelling can be well explained by the consideration of sustained heating as a model parameter during the decay phase of the flare. Therefore, in this study, we consider the loop length estimated from the hydrodynamic loop modelling as more accurate than that from the quasi-static loop model. The estimated loop-length is also found to be of a similar order to other RS CVn-type binaries (see Agrawal, Rao & Riegler 1986; Güdel et al. 1999; Osten et al. 2003; Pandey & Singh 2012; Tsuboi et al. 2016; Sasaki et al. 2021).

We cannot spatially resolve the flare location on the SZ Psc system. However, with the estimated loop length, we can have some idea about the flare location. The separation of the binary components,

as estimated using *Gaia* DR2 observations, is found to be 3.53 AU (see Kervella et al. 2019), which is $\sim$84 times that of the estimated loop-length of the flare. It is unlikely that the magnetic field lines responsible for the flare were inter-binary loops as found in a few RS CVn binaries (see Uchida & Sakurai 1983). The flare is likely to be associated with just one of the stellar components. The flaring loop height of the flare on SZ Psc was estimated to be 57 per cent of the radius of the K1 IV primary, whereas it is 192 per cent of the radius of the F8 V secondary. As the estimated total magnetic field strength that would be required to accumulate the emitted energy and to keep the plasma confined in a stable magnetic loop configuration is $\sim$490 G, it is expected that a strong magnetic dynamo is present on the stellar component that is associated with the flare. Several studies have shown that the F-type stars are less active than the K-type stars due to their thinner convective envelop (e.g. Schrijver 1983; Karmakar et al. 2016; Savanov et al. 2016, 2018b, 2019; Karmakar & Pandey 2018; Karmakar 2019; Karmakar et al. 2019). Therefore, it is more likely that the K-type primary component is responsible for such a high level of magnetic activity. Moreover, with the high-rotational velocity of each component due to being a tidally locked system, since the subgiant primary component has a thicker convection zone than the main-sequence secondary component, it is more likely that this large flare was associated with the primary component.

8.2 Flare duration versus energy on RS CVn-type binaries

As described in Section 3, at the beginning of the observation, the flare on SZ Psc was already in the rising phase with a *Swift* XRT count rate of $\sim$79 count s^{-1}. Therefore, we could not estimate the total duration of the flare precisely. However, with the estimated flare duration of >31 h, this flare is identified as one of the longest duration X-ray flares on SZ Psc. Using MAXI/GCS instrument, another long-duration flare on SZ Psc was detected in 2–20 keV band (see fig. 1 of Tsuboi et al. 2016, where FN14 represents the flare on SZ Psc). However, due to the large temporal uncertainty ($\sim$8 h) in the MAXI/GCS observation, the duration of the flares is difficult to compare quantitatively.

The observed flare duration in SZ Psc is large as compared to those of solar-type stars or main-sequence binaries (see Pandey & Singh 2008; Pandey & Karmakar 2015; Savanov et al. 2018a; Karmakar et al. 2022). However, it is well among the flare duration for RS CVn-type binaries which ranges from a few minutes to several days (e.g. Franciosini et al. 2001; Pandey & Singh 2012; Gong et al. 2016; Sasaki et al. 2021). We also estimated the total energy released during the flare is $2.1 \pm 0.3 \times 10^{38}$ erg. This is very large in comparison to the total energy of the X-ray superflares on the solar-type stars (see Favata et al. 2000; Osten et al. 2010; Karmakar et al. 2017). Recent studies have shown that the RS CVn stars release energy in the range of 10^{34} to 10^{40} erg during flares (see Endl et al. 1997; Franciosini et al. 2001; Pandey & Singh 2012; Tsuboi et al. 2016; Sasaki et al. 2021).

In Fig. 10(a), we have plotted the flare duration of the RS CVn-type binaries with the flare energies as derived in the literature (see legends 1–6 in Fig. 10). We converted the observed X-ray flux into the 0.35–10 keV energy band using webpimms.[15] For the conversion, we considered the best-known coronal parameters and utilized those in the multitemperature astrophysical plasma models. We found that a positive correlation exists between the flare duration and flare energy of the RS CVn binaries in the soft X-ray band. We computed a
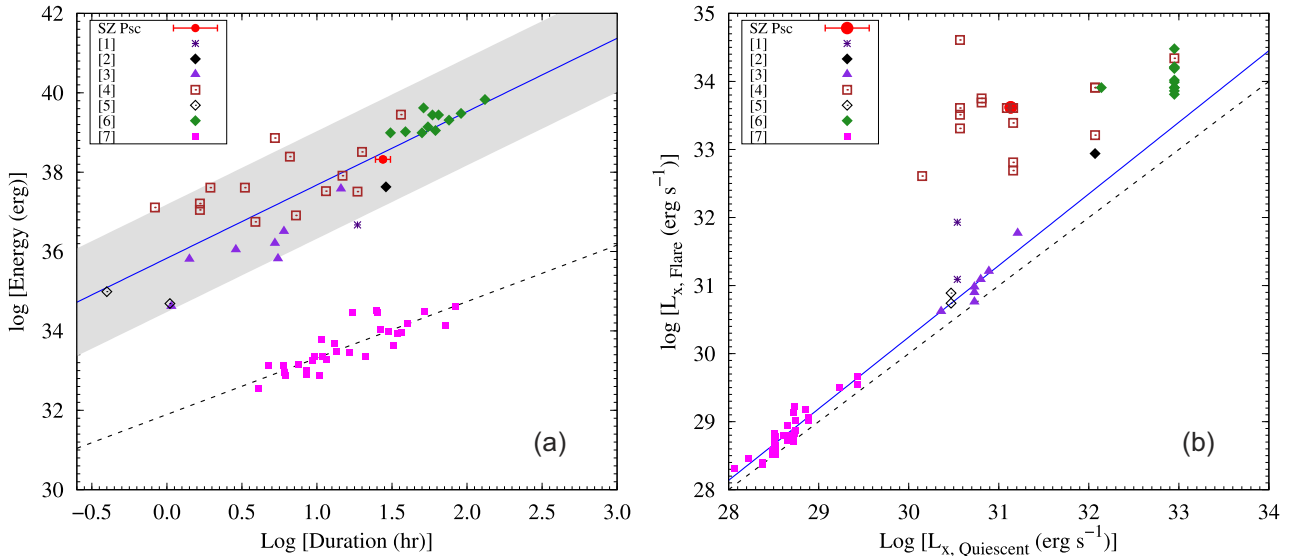
---

[15]https://heasarc.gsfc.nasa.gov/cgi-bin/Tools/w3pimms/w3pimms.pl

Figure 10. (a) Flare duration versus flare energy and (b) Flare luminosity versus quiescent luminosity are shown. The flare on SZ Psc, investigated in this study, is shown with the solid red circle. We have compared the flares on the RS CVn-type binary systems from the literature with different symbols. Figure legends: [1]: Large X-ray flare on HU Vir (Endl, Strassmeier & Kurster 1997), [2]: BeppoSAX observation of a large flare on UX Ari (Franciosini, Pallavicini & Tagliaferri 2001), [3]: Seven flares from five RS CVn-type binaries (UZ Lib, σ Gem, λ And, V711 Tau, and EI Eri; Pandey & Singh 2012), [4]: 13 flares eight RS CVn systems (VY Ari, UX Ari, HR1099, GT Mus, V841 Cen, AR Lac, SZ Psc, and II Peg; Tsuboi et al. 2016), [5]: Two flares on XY Uma (Gong et al. 2016), [6]: 11 flares on GT Mus (Sasaki et al. 2021), [7]: 30 flares observed with *Extreme Ultraviolet Explorer* (EUVE) in nine RS CVn-type binary systems (σ^2 CrB, V824 Ara, V815 Her, AR Lac, BH CVn, V711 Tau, UX Ari, II Peg, λ And, VY Ari, and AR Psc; Osten & Brown 1999). All the X-ray luminosities and energies are converted to 0.35–10 keV energy range using the `webpimms` with multitemperature `apec` model, considering the nearest corresponding temperature components. In panel (a), the solid blue line indicates the derived relation between flare duration versus flare energy in soft X-ray (0.35–10 keV energy band) as discussed in Section 8. The black dashed line shows the empirical limit for the flares on RS CVn binaries as observed in EUV observations (Osten & Brown 1999). In panel (b), the solid blue line indicates the empirical limit for EUV observations adopted from Osten & Brown (1999), whereas the black dashed line is a line of equality between the two luminosities.

linear Pearson correlation coefficient of 0.84 between the duration and flare energies, with a null hypothesis probability of 9.13×10^{-9}. We further derived the relationship between the flare energy (in the 0.35–10 keV band) and the flare duration of the RS CVn-type binary systems as follows.

$$\log_{10}\left(\frac{\mathrm{E_{tot}}}{\mathrm{erg}}\right) = (1.8 \pm 0.2) \times \log_{10}\left(\frac{\mathrm{Dn}}{\mathrm{h}}\right) + (35.8 \pm 0.2) \qquad (8)$$

The blue solid line in Fig. 10(a) shows the best-fitting line with reduced χ^2 value of 0.7 (for 34 dof). The grey shaded region represents the 1σ variations. It is found that the flare on SZ Psc is also following the relationship between energy and flare duration. In Fig. 10(a), the solid pink squares (legend 7) indicate the energy versus duration relation observed in the EUV energy band adapted from Osten & Brown (1999). The black dashed line shows the derived relationship between the flare energy in EUV and the flare duration corresponding to $\mathrm{E_{flare}} \propto \mathrm{Dn}^{1.42}$. This power-law index is in good agreement (within 1σ) with the derived relationship given in equation (8). However, the energy budget for the soft X-ray (0.35–10 keV) in the flares in RS CVn binaries is found to be a 100 times more than the EUV counterpart.

8.3 Quiescent versus flaring X-ray emission

Using *XMM–Newton* and *Swift* observations in the 0.35–10 keV energy band, we found that the quiescent corona of SZ Psc can be well described by three temperature plasma with estimated temperatures of 4.1, 13.1, and 47.6 MK. This is the first time a detailed analysis of the quiescent corona of SZ Psc has been performed in the soft X-ray energy band. Using the IPC of the *Einstein Observatory* in the 0.2–4 keV energy range, Majer et al. (1986) assumed that the corona of SZ Psc consists of a single-temperature plasma, and the temperature was estimated to be 7.44–7.58 MK. From the *ROSAT* all-sky survey observations in the 0.1–2.4 keV energy band, Dempsey et al. (1993) reported that the corona of SZ Psc consists of two temperature plasma, with the derived temperatures of 1.2 and 16.6 MK. A few RS CVn-type binaries are also found to have three temperature quiescent corona (e.g. UX Ari, V711 Tau, and EI Eri; Güdel et al. 1999; Pandey & Singh 2012).

The time-resolved spectroscopy (this work) shows that the flare temperature varies with time, and the observed peak flare temperature is derived to be 199 MK. Using MAXI/GCS observations Tsuboi et al. (2016) estimated the temperature of a flare on SZ Psc to be >23.2 MK. For RS CVn binaries, the flare temperatures have been estimated to be 25–300 MK (Güdel 2004; Osten et al. 2007; Pandey & Singh 2012), whereas the temperature is also similar to those of the superflares (Favata et al. 2000; Maggio et al. 2000; Osten et al. 2010; Karmakar et al. 2017). We found a delay between the temperature and the emission measure peaks. Similar delays have been observed in the solar and stellar flares (Van den Oord & Mewe 1989; Sylwester et al. 1993; Stelzer et al. 2002).

At the beginning of the flare, when the possible reconnection event leads to the release of the stored magnetic energy as kinetic energy, the temperature of the newly formed loop reaches its maximum near the loop top. In the later part of the flare, the temperature generally decreases as the heat is transmitted via the radiative and conductive
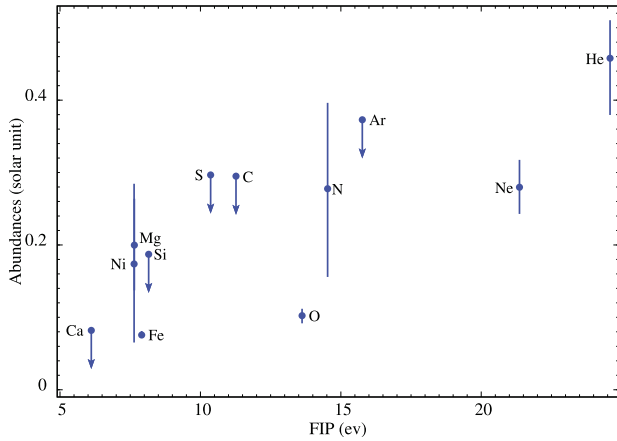
Figure 11. Elemental abundances relative to solar photospheric values (Anders & Grevesse 1989) as a function of the FIP during quiescence (Q2 segment) of SZ Psc. The elemental abundances show an inverse-FIP effect.

cooling process. Thus, the temperature peaks at the beginning of the flare. When the heat pulse reaches the chromospheric footpoint and the denser chromospheric material gets evaporated, the density of the coronal loop and hence the emission measure is found to be increased. Therefore, emission measure peak is found to be delayed with respect to the temperature peak. The emission measure near the flare peak is found to be ∼97 times that of the minimum value. The increase in density indicates a large amount of evaporation of chromospheric material within the flaring loop during the flare.

The peak X-ray luminosity of the flare on SZ Psc is estimated as 4.2×10^{33} erg s^{-1}, which is ∼306 times more than its quiescent luminosity. Previously, two flares have been observed on SZ Psc using MAXI/GSC instrument in the 2–20 keV band. The peak luminosity during those flares were estimated as 5×10^{32} erg s^{-1} (detected on 2009 September 28; Tsuboi et al. 2016), and 3×10^{33} erg s^{-1} (detected on 2011 November 5; Negoro et al. 2011). We plotted the flare luminosities versus quiescent luminosities of RS CVn binaries in Fig. 10(b). The legends [1–6] show the quiescent and flare luminosity of RS CVn binaries in the 0.35–10 keV band, whereas EUV observations from Osten & Brown (1999) are also plotted with pink squares (legend 7). We did not find any correlation between the luminosities of the flares and the quiescent states in X-ray bands. A similar thing was also noticed for the solar case, where the flare luminosities vary within a wide range of distribution. The solid blue line in Fig. 10(b) showing a linear relationship between the EUV flaring and quiescent luminosities, as adopted from Osten & Brown (1999), might be due to a selection or detection bias.

8.4 Metallic abundances

Using *XMM–Newton* RGS spectra, we estimated the elemental abundances of heavy elements. In Fig. 11, the elemental abundances with respect to solar photospheric abundances are plotted against the first ionization potential (FIP) of the corresponding element. For the stars like the Sun, it has been observed that the low-FIP elements like Fe, Si, and Mg are three to four times more abundant in the corona when compared to high-FIP elements like C, N, O, and Ne. This phenomenon is known as coronal FIP bias (e.g. see Feldman 1992; Del Zanna & Mason 2014). A reversed pattern (i.e. enhanced high-FIP elements when compared to the low-FIP elements) is frequently observed in active stars (e.g. see Brinkman et al. 2001; Audard et al. 2003). From Fig. 11, we identified that the abundance pattern of the

quiescent corona of SZ Psc indicates an inverse-FIP effect. Several theoretical studies attempted to explain the FIP bias (see Hénoux 1998). The latest model is based on the Ponderomotive force model (Laming 2015, 2021), which is able to reproduce the overall features of both the FIP and inverse-FIP bias. The findings of the inverse-FIP effect on the quiescent corona of SZ Psc can be explained using this model.

Due to the non-availability of high-resolution spectra during the flare, we could not carry out a quantitative study of the temporal evolution of the individual chemical abundances during the flare. However, the global metallic abundance of the flaring corona is found to vary during the flare. In the rising phase of the flare, the abundance seems to increase from 0.4 $Z_\odot$ to 0.6 $Z_\odot$. However, considering the uncertainty level, this increase is not significant. In the decay phase of the flare, the abundance is found to decrease significantly up to ∼0.1 $Z_\odot$. In the case of other RS CVn binaries such as σ Gem, V711 Tau, EI Eri, II Peg, UX Ari, and $σ^2$ Crb, the metallic abundances have also been found to vary during the flaring events (see Mewe et al. 1997; Güdel et al. 1999; Osten et al. 2003; Nordon & Behar 2008; Pandey & Singh 2012). The variation of metallic abundances during the flare on SZ Psc is found to be consistent with the previously observed behaviour. At the beginning of the event, fresh chromospheric material is supposed to be evaporated in the flaring loops, which results in the enhancement of its abundance. During the decay phase of the flare, the fractionation mechanism is considered to be responsible for lower abundances observed in the coronal plasma until it reaches the quiescent state value (Favata & Micela 2003).

DATA AVAILABILITY

The data underlying this article are available in the HEASARC archive (https://heasarc.gsfc.nasa.gov/db-perl/W3Browse/w3browse.pl), *XMM–Newton* archive (http://nxsa.esac.esa.int/nxsa-web/search), and *Swift* archive (https://heasarc.gsfc.nasa.gov/cgi-bin/W3Browse/swift.pl).

REFERENCES

Agrawal P. C., Rao A. R., Riegler G. R., 1986, MNRAS, 219, 777
Anders E., Grevesse N., 1989, Geochim. Cosmochim. Acta, 53, 197
Antonopoulou E., Deliyannis J., Mitrou C. K., 1995, Inf. Bull. Var. Stars, 4262, 1

Arnaud K. A., 1996, in Jacoby G. H., Barnes J., eds, ASP Conf. Ser., Astronomical Data Analysis Software and Systems V. Astron. Soc. Pac., San Francisco, Vol. 101, p. 17

Aschwanden M. J., Alexander D., 2001, Sol. Phys., 204, 91

Aschwanden M. J., Stern R. A., Güdel M., 2008, ApJ, 672, 659

Audard M., Güdel M., Sres A., Raassen A. J. J., Mewe R., 2003, A&A, 398, 1137

Ayres T. R., Brown A., Harper G. M., Osten R. A., Linsky J. L., Wood B. E., Redfield S., 2003, ApJ, 583, 963

Bailer-Jones C. A. L., Rybizki J., Fouesneau M., Mantelet G., Andrae R., 2018, AJ, 156, 58

Barthelmy S. D. et al., 2005, Space Sci. Rev., 120, 143

Bopp B. W., Noah P., Klimke A., Hall D. S., Henry G. W., 1981, PASP, 93, 504

Brinkman A. C. et al., 2001, A&A, 365, L324

Burrows D. N. et al., 2005, Space Sci. Rev., 120, 165

Cao D. et al., 2019, MNRAS, 482, 988

Cao D.-T., Gu S.-H., 2012, A&A, 538, A130

Catalano S., Frisina A., Rodono M., Scaltriti F., 1978, Inf. Bull. Var. Stars, 1427, 1

Crespo-Chacón I., Micela G., Reale F., Caramazza M., López-Santiago J., Pillitteri I., 2007, A&A, 471, 929

D'Elia V., de Pasquale M., Evans P. A., Krimm H. A., Maselli A., Page K. L., Sakamoto T., Sbarufatti B., 2015, GRB Coord. Netw., 17303, 1

Del Zanna G., Mason H. E., 2014, A&A, 565, A14

Dempsey R. C., Linsky J. L., Schmitt J. H. M. M., Fleming T. A., 1993, ApJ, 413, 333

Den Herder J. W. et al., 2001, A&A, 365, L7

Doyle J. G., Mitrou C. K., Mathioudakis M., Antonopoulou E., 1994, A&A, 283, 522

Drake S. A., Osten R. A., Krimm H., De Pasquale M., Gehrels N., Barthelmy S., 2015, Astron. Telegram, 6940,1

Eaton J. A., Hall D. S., 1979, ApJ, 227, 907

Eaton J. A., Henry G. W., 2007, PASP, 119, 259

Eaton J. A., Scaltriti F., Cerruti-Sola M., Sarma M. B. K., Ausekar B. D., Catalano S., Rodono M., 1982, Ap&SS, 82, 289

Endl M., Strassmeier K. G., Kurster M., 1997, A&A, 328, 565

Favata F., Micela G., 2003, Space Sci. Rev., 108, 577

Favata F., Reale F., Micela G., Sciortino S., Maggio A., Matsumoto H., 2000, A&A, 353, 987

Favata F., Flaccomio E., Reale F., Micela G., Sciortino S., Shang H., Stassun K. G., Feigelson E. D., 2005, ApJS, 160, 469

Feldman U., 1992, Phys. Scr., 46, 202

Franciosini E., Pallavicini R., Tagliaferri G., 2001, A&A, 375, 196

Gabriel A. H., Jordan C., 1969, Nature, 221, 947

Getman K. V., Feigelson E. D., Broos P. S., Micela G., Garmire G. P., 2008, ApJ, 688, 418

Getman K. V., Broos P. S., Salter D. M., Garmire G. P., Hogerheijde M. R., 2011, ApJ, 730, 6

Getman K. V., Feigelson E. D., Garmire G. P., 2021, ApJ, 920, 154

Godet O. et al., 2009, A&A, 494, 775

Gong H., Osten R., Maccarone T., Reale F., Liu J.-F., Heckert P. A., 2016, Res. Astron. Astrophys., 16, 131

Güdel M., 2004, A&AR, 12, 71

Güdel M., Linsky J. L., Brown A., Nagase F., 1999, ApJ, 511, 405

Hall D. S., 1976, in Fitch W. S., ed., Astrophysics and Space Science Library, IAU Colloq. 29: Multiple Periodic Variable Stars. Springer-Verlag, Berlin, 60, 287

Hénoux J.-C., 1998, Space Sci. Rev., 85, 215

HI4PI Collaboration, 2016, A&A, 594, A116

Huenemoerder D. P., Ramsey L. W., 1984, AJ, 89, 549

Jakate S., Bakos G. A., Fernie J. D., Heard J. F., 1976, AJ, 81, 250

Jansen F. et al., 2001, A&A, 365, L1

Jensch A., 1934, Astron. Nachr., 252, 393

Kang Y. W., Lee W.-B., Kim H.-i., Oh K.-D., 2003, MNRAS, 344, 1227

Karmakar S., 2019, Evolution of Magnetic Activities in Late-Type Stars, PhD thesis, ARIES, Nainital, India; PRSU, Raipur, India, 1, 1,

Karmakar S., Pandey J. C., 2018, Bull. Soc. R. Sci. Liege, 87, 163

Karmakar S. et al., 2016, MNRAS, 459, 3112

Karmakar S., Pandey J. C., Airapetian V. S., Misra K., 2017, ApJ, 840, 102

Karmakar S., Pandey J. C., Naik S., Savanov I. S., Raj A., 2019, Bull. Soc. R. Sci. Liege, 88, 182

Karmakar S., Naik S., Pandey J. C., Savanov I. S., 2022, MNRAS, 509, 3247

Kervella P., Arenou F., Mignard F., Thévenin F., 2019, A&A, 623, A72

Laming J. M., 2015, Living Rev. Sol. Phys., 12, 2

Laming J. M., 2021, ApJ, 909, 17

Lanza A. F., Rodonò M., Mazzola L., Messina S., 2001, A&A, 376, 1011

Maggio A., Pallavicini R., Reale F., Tagliaferri G., 2000, A&A, 356, 627

Majer P., Schmitt J. H. M. M., Golub L., Harnden F. R., Jr., Rosner R., 1986, ApJ, 300, 360

Mason K. O. et al., 2001, A&A, 365, L36

Mewe R., Kaastra J. S., van den Oord G. H. J., Vink J., Tawara Y., 1997, A&A, 320, 147

Moretti A. et al., 2005, in Siegmund O. H. W., ed., Proc. SPIE Conf. Ser., UV, X-Ray, and Gamma-Ray Space Instrumentation for Astronomy XIV. SPIE, Bellingham, Vol 5898, p. 360

Negoro H. et al., 2011, Astron. Telegram, 3737

Nordon R., Behar E., 2008, A&A, 482, 639

Osten R. A., Brown A., 1999, ApJ, 515, 746

Osten R. A., Ayres T. R., Brown A., Linsky J. L., Krishnamurthi A., 2003, ApJ, 582, 1073

Osten R. A., Drake S., Tueller J., Cummings J., Perri M., Moretti A., Covino S., 2007, ApJ, 654, 1052

Osten R. A. et al., 2010, ApJ, 721, 785

Pagani C. et al., 2011, A&A, 534, A20

Pandey J. C., Karmakar S., 2015, AJ, 149, 47

Pandey J. C., Singh K. P., 2008, MNRAS, 387, 1627

Pandey J. C., Singh K. P., 2012, MNRAS, 419, 1219

Parker E. N., 1988, ApJ, 330, 474

Ramsey L. W., Nations H. L., 1981, PASP, 93, 732

Reale F., 2007, A&A, 471, 271

Reale F., Betta R., Peres G., Serio S., McTiernan J., 1997, A&A, 325, 782

Reale F., Güdel M., Peres G., Audard M., 2004, A&A, 416, 733

Romano P. et al., 2006, A&A, 456, 917

Roming P. W. A. et al., 2005, Space Sci. Rev., 120, 95

Rosner R., Tucker W. H., Vaiana G. S., 1978, ApJ, 220, 643

Sasaki R. et al., 2021, ApJ, 910, 25

Savanov I. S. et al., 2016, Acta Astron., 66, 381

Savanov I. S., Dmitrienko E. S., Karmakar S., Pandey J. C., 2018a, Astron. Rep., 62, 532

Savanov I. S., Dmitrienko E. S., Pandei D. S., Karmakar S., 2018b, Astrophys. Bull., 73, 454

Savanov I. S., Naroenkov S. A., Nalivkin M. A., Pandey J. C., Karmakar S., 2019, Astron. Lett., 45, 602

Schmitt D., 1994, in Belvedere G., Rodono M., Simnett G. M., eds, Lecture Notes in Physics, Vol.432, Advances in Solar Physics. Springer-Verlag, Berlin, p. 61

Schrijver C. J., 1983, A&A, 127, 289

Smith R. K., Brickhouse N. S., Liedahl D. A., Raymond J. C., 2001, ApJ, 556, L91

Spitzer L., 1965, Physics of Fully Ionized Gases. 2nd rev., Interscience Tracts on Physics and Astronomy, Interscience Publication, Vol. 1, New York, p. 1

Stelzer B. et al., 2002, A&A, 392, 585

Strüder L. et al., 2001, A&A, 365, L18

Sylwester B., Sylwester J., Serio S., Reale F., Bentley R. D., Fludra A., 1993, A&A, 267, 586

Tsuboi Y. et al., 2016, PASJ, 68, 90

Tumer O., Kurutac M., 1979, Inf. Bull. Var. Stars, 1547, 1

Tunca Z., 1984, Ap&SS, 105, 23

Turner M. J. L. et al., 2001, A&A, 365, L27

Uchida Y., Sakurai T., 1983, in Byrne P. B., Rodono M., eds, Astrophysics and Space Science Library, IAU Colloq. 71: Activity in Red-Dwarf Stars. Springer-Verlag, Berlin, Vol102, p. 629

Van den Oord G. H. J., Mewe R., 1989, A&A, 213, 245

Walter F. M., Bowyer S., 1981, ApJ, 245, 671

Wilms J., Allen A., McCray R., 2000, ApJ, 542, 914

Xiang Y., Gu S., Cameron A. C., Barnes J. R., Zhang L., 2016, MNRAS, 456, 314

Zhang L.-Y., Gu S.-H., 2008, A&A, 487, 709

SUPPORTING INFORMATION

Supplementary data are available at *MNRAS* online.

Figure 12. The online-only material related to Fig. 6 of this article: Time-resolved *Swift* XRT spectra of SZ Psc in 0.35–10 keV energy band are shown for all the individual segments. In the top panel of each figure, the spectra have been shown with grey plus symbols. The spectra have been extracted for a minimum of 20 counts per bin. The labels (black) in the left-bottom corner of each panel indicate the segment numbers. The start-time and end-time corresponding to each time segment is given in the second column of Table 4. The time evolution of the spectra in each segment is clearly visible. The quiescent segment 'Q1' has been best fitted with a 3-T astrophysical plasma model (apec), whereas all the time-resolved segments during the flare have been fitted with a 4-T apec model. The best-fitting spectra have been shown with the solid red line. The bottom panel shows the residual in the unit of $\Delta\chi^2$. Please see the text for a detailed explanation.

Please note: Oxford University Press is not responsible for the content or functionality of any supporting materials supplied by the authors. Any queries (other than missing material) should be directed to the corresponding author for the article.

This paper has been typeset from a TeX/LaTeX file prepared by the author.